

Ground-based CCD astrometry with wide field imagers.*

III. WFI@2.2m proper-motion catalog of the globular cluster ω Centauri.

Bellini, A.^{1,2}, Piotto, G.¹, Bedin, L. R.², Anderson, J.², Platais, I.³, Momany, Y.⁴, Moretti, A.⁴, Milone, A. P.¹, and Ortolani, S.¹

- ¹ Dipartimento di Astronomia, Università di Padova, Vicolo dell'Osservatorio 3, I-35122 Padova, Italy
e-mail: [andrea.bellini;giampaolo.piotto;alessia.moretti;antonino.milone;sergio.ortolani]@unipd.it
- ² Space Telescope Science Institute, 3700 San Martin Drive, Baltimore, MD 21218, USA
e-mail: [bellini;bedin;jayander]@stsci.edu
- ³ Dept. of Physics and Astronomy, The Johns Hopkins University, Baltimore, MD 21218, USA
e-mail: imants@pha.jhu.edu
- ⁴ INAF: Osservatorio Astronomico di Padova, vicolo dell'Osservatorio 5, 35122 Padova, Italy
e-mail: yazan.almomany@oapd.inaf.it

Received 1 September 2008 / Accepted 3 October 2008

ABSTRACT

Context. ω Centauri is the most well studied Galactic Globular Cluster because of its numerous puzzling features: significant dispersion in metallicity, multiple populations, triple main-sequence, horizontal branch morphology, He-rich population(s), and extended star-formation history. Intensive spectroscopic follow-up observing campaigns targeting stars at different positions in the color-magnitude diagram promises to clarify some of these peculiarities.

Aims. To be able to target cluster members reliably during spectroscopic surveys and both spatial and radial distributions in the cluster outskirts without including field stars, a high quality proper-motion catalog of ω Cen and membership probability determination are required. The only available wide field proper-motion catalog of ω Cen is derived from photographic plates, and only for stars brighter than $B \sim 16$. Using ESO archive data, we create a new, CCD-based, proper-motion catalog for this cluster, extending to $B \sim 20$.

Methods. We used high precision astrometric software developed specifically for data acquired by WFI@2.2m telescope and presented in the first paper of this series. We demonstrated previously that a 7 mas astrometric precision level can be achieved with this telescope and camera for well exposed stars in a single exposure, assuming an empirical PSF and a local transformation approach in measuring star displacements.

Results. We achieved a good cluster-field separation with a temporal base-line of only four years. We corrected our photometry for sky-concentration effects. We provide calibrated photometry for $UBVR_{CI}$ wide-band data plus narrow-band filter data centered on H_{α} for almost 360 000 stars. We confirm that the ω Cen metal-poor and metal-rich components have the same proper motion, and demonstrate that the metal-intermediate component in addition exhibits the same mean motion as the other RGB stars. We provide membership probability determinations for published ω Cen variable star catalogs.

Conclusions. Our catalog extends the proper-motion measurements to fainter than the cluster turn-off luminosity, and covers a wide area ($\sim 33' \times 33'$) around the center of ω Cen. Our catalog is electronically available to the astronomical community.

Key words. Globular clusters: general – Globular clusters: individual (ω Cen) – Stars: populations II, H-R diagram – Catalogs – Astrometry

1. Introduction

The globular cluster ω Centauri (ω Cen) is the most luminous and massive cluster in the Galaxy. Observational evidence collected over the years has indicated that ω Cen is also the most puzzling stellar system in terms of stellar content, structure, and kinematics. Probably the most well studied of its peculiarities is one related to its stellar metallicity distribution (Norris & Bessell 1975; 1977; Freeman & Rodgers 1975; Bessell & Norris 1976; Butler et al. 1978; Norris & Da Costa 1995; Suntzeff & Kraft 1996; Norris et al. 1996). There is a significant dispersion in the iron abundance distribution of ω Cen, with a primary peak about $[\text{Fe}/\text{H}] \sim -1.7$ – -1.8 and a long tail, extend-

ing to $[\text{Fe}/\text{H}] \sim -0.6$, which contains another 3-4 secondary peaks. It is possible to identify these metallicity peaks with distinct stellar populations (Pancino et al. 2000; Rey et al. 2004; Sollima et al. 2005; Villanova et al. 2007). Ground-based (Lee et al. 1999; Pancino et al. 2000) and *Hubble Space Telescope* (HST) (Anderson 1997; Bedin et al. 2004; Ferraro et al. 2004) photometry show clearly that ω Cen hosts different stellar populations. In particular, Pancino et al. (2000) demonstrated that the ω Cen red giant branch (RGB) consists of at least four distinct branches, spanning a wide range of metallicity. On the other hand, the ω Cen sub giant branch (SGB) has an intricate web of 5 distinct sequences, indicating an extended range of metallicity and age (see Bedin et al. 2004; Hilker et al. 2004; Sollima et al. 2005; Stanford et al. 2006; Villanova et al. 2007).

Anderson (1997), Bedin et al. (2004), and Villanova et al. (2007), by studying fainter stars with deep and high resolution HST photometry, demonstrated that the main sequence (MS) is

Send offprint requests to: Bellini, A.

* Based on archive observations with the MPI/ESO 2.2m telescope, located at La Silla and Paranal Observatory, Chile.

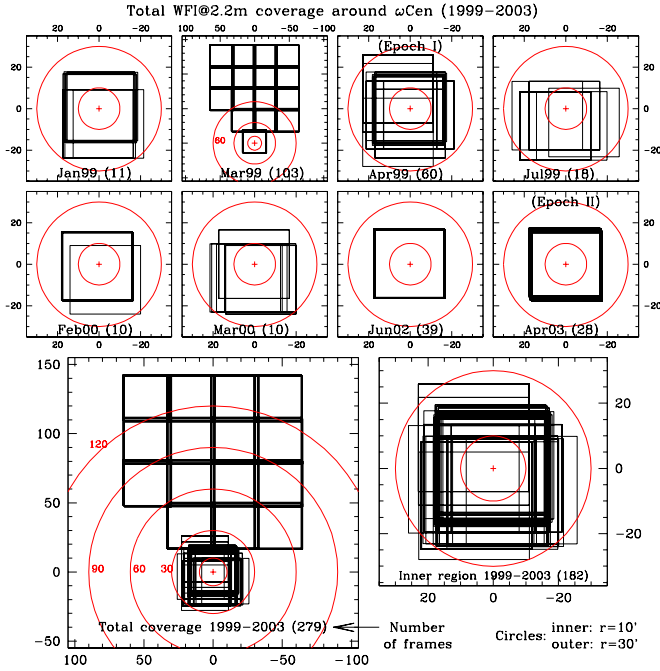


Fig. 1. Position footprint of the entire sample of WFI images around the ω Cen center (marked with a “+”). The first two rows show the covered areas sorted by month and year. In the lower panels of the figure, the total coverage of all of the 279 images (on the left), and a zoom-in of the central part of the cluster (on the right) are shown. The numbers in parenthesis after the dates represent the total number of images for that observing run. North is up, East to the left.

divided into 3 distinct sequences. The spectroscopic study of the MS stars of ω Cen by Piotto et al. (2005) showed that the bluest of the main sequences is more metal rich than any of the redder sequences, which increased the ambiguity surrounding the cluster. An overabundance of He in the blue MS could reproduce the ω Cen MS photometric and spectroscopic properties (Bedin et al. 2004; Norris 2004; Piotto et al. 2005), although the origin of the puzzling MS morphology is still far from being understood.

A deeper insight into the enigmatic stellar populations of ω Cen should combine a deep, high resolution analysis of the inner and most crowded regions, with a wide field observations of the outskirts. While the first type of data has been provided adequately by *HST*, wide field coverage of ω Cen requires ground-based data which are more difficult to obtain. Acquisition of data for a wider field-of-view will inevitably result in higher contamination by Galactic foreground/background populations. The only reasonable and efficient way to decontaminate the ω Cen outer stellar populations is by means of proper-motion analyses that help to isolate the Galactic contribution. The only available wide field ω Cen proper-motion catalog (van Leeuwen et al. 2000, hereafter vL00) is based on photographic observations and only provides measurements for stars brighter than $B \sim 16$. In this paper, we attempt to provide the first CCD-based proper motion catalog of ω Cen, extending the cleaned stellar populations down to $B \sim 20$, i.e. 4 mag. deeper than vL00.

In the first paper of this series, Anderson et al. (2006), hereafter Paper I, demonstrated that WFI@2.2m observations, with a time base-line of only a few years, allow a successful separation of cluster members from Galactic field stars in the two GCs closest to the Sun: NGC6121 and NGC6397. In this paper, we

Table 1. Description of the data set used for the WFI@2.2m catalog.

filter	t_{exp}	seeing	airmass
January, 1999			
B_{842}	3×30s, 1×300s;	1".0-1".3	~ 1.20
658nm	1×120s, 5×180s, 1×900s;	1".0-1".3	1.15-1.18
March, 1999			
V_{843}	52×200s;	0".8-1".2	1.1-1.2
I_{845}	51×150s;	0".7-1".5	1.1-1.45
April, 1999			
R_{844}	1×5s, 1×10s, 1×15, 1×30, 5×60s;	1".0-1".3	1.3-1.6
I_{845}	1×5s, 1×10s, 1×20s, 1×45s, 4×90s;	0".74-1".7	1.4-1.9
658nm	2×30, 4×120, 5×180s;	0".8-1".15	1.1-1.2
(epoch I)			
B_{842}	1×15s, 1×30s, 1×60s, 5×120s;	0".75-1".3	1.2-1.5
V_{843}	3×5s, 3×10s, 1×15s, 2×20s;	0".7-1".0	1.2-1.6
	1×30s, 4×45s, 10×90s;	0".76-1".36	1.1-1.5
July, 1999			
U_{877}	2×1800s;	1".4-1".6	~ 1.14
B_{842}	1×10s, 1×30s, 1×40s, 1×300s;	1".4-1".8	1.14-1.25
V_{843}	1×10s, 1×20s, 1×150s, 1×240s;	1".3-1".6	1.15-1.25
I_{845}	1×10s, 2×20s, 1×240s;	1".13-1".6	1.17-1.25
658nm	3×120s, 1×1200s;	1".13-1".5	1.18-1.23
February, 2000			
B_{842}	2×30s, 2×240s;	1".45-1".7	~ 1.13
V_{843}	1×30s, 2×240s;	1".1-1".2	~ 1.13
I_{845}	1×30s, 2×240s;	~ 1".0	~ 1.13
March, 2000			
U_{841}	4×300s, 1×2400s;	1".1-1".2	1.17-1.38
V_{843}	5×30s;	0".9-1".4	~ 1.45
June, 2002			
U_{877}	4×30s, 7×300s;	0".8-2".0	1.14-1.18
B_{878}	1×5s, 3×8s, 9×60s;	0".8-1".5	1.13-1.16
V_{843}	3×5s, 3×40s, 3×60s;	0".75-2".0	~ 1.13
I_{845}	3×20s, 3×40s;	0".7-1".4	~ 1.13
April, 2003 (epoch II)			
B_{878}	7×40s; 7×120s;	0".7-0".9	1.14-1.16
V_{843}	7×40s; 7×120s;	0".8-1".0	1.13

apply the high precision astrometric and photometric techniques developed by Paper I to all available WFI@2.2m archive data of ω Cen.

In Sect. 2, we describe the available WFI observations of ω Cen, and the data sets that we used to derive proper motions. In Sect. 3, we discuss our photometric data reduction technique, the sky-concentration effect minimization, and the photometric calibration. In Sect. 4, we describe in detail how we treated the differential chromatic refraction (DCR) effects between the two epochs. Membership probability is discussed in Sect. 5, while in Sect. 6 we outline possible applications of our catalog. Finally, in Sect. 7, we summarize our results and describe the electronic catalog.

Table 2. Characteristics of the used filters (from WFI manual) λ_c =central wavelength, FWHM=Full Width at Half Maximum, λ_p =transmission peak wavelength, T_p =transmission percentage at peak level. (*) LWP means Long Wave Pass: in this case the cutoff limit is determined by the CCD quantum efficiency.

Wide-band filters				
Name	λ_c [nm]	FWHM [nm]	λ_p [nm]	T_p [%]
U_{877} (U/50)	340.4	73.2	350.3	82.35
U_{841} (U/38)	363.7	38.3	362.5	51.6
B_{878} (B/123)	451.1	133.5	502.5	88.5
B_{842} (B/99)	456.3	99.0	475.0	91.2
V_{843} (V/89)	539.6	89.4	523.0	87.0
R_{844} (R _C)	651.7	162.2	668.5	93.9
I_{845} (I _C /lwp)	783.8	LWP*	1001.0	97.6
Narrow-band filters				
Name	λ_c [nm]	FWHM [nm]	λ_p [nm]	T_p [%]
658nm (H_α)	658.8	10.3	504.0	90.7

2. Observations

We used a collection of 279 archive images acquired between January 20, 1999 and April 14, 2003 at the ESO/MPI2.2m telescope at La Silla (Chile) equipped with the wide-field imager camera (WFI). A detailed log of observations is reported in Table 1. This camera, which consists of an array mosaic of 4×2 chips, 2141×4128 pixels each, has a total field of view of $34' \times 33'$, and a pixel scale of $0.238''/\text{pixel}$. More details of the instrumental setup were given in Paper I. Images were obtained using U, B, V, R_C, I_C wide-band and 658nm (H_α) narrow-band filters, whose characteristics are summarized in Table 2.

For the derivation of proper motions, we used only B and V images acquired in April 1999 and April 2003 (see Sect. 4 for further details of this choice). The total field-of-view covered by the entire sample is indicated in Fig. 1, where axis coordinates are $(\Delta\alpha \cos \delta, \Delta\delta)$, expressed in units of arcmin from the ω Cen center (North is up, East is to the left). Concentric circles have diameters, if not specified, of $10'$ (inner circle) and $30'$ (outer circle), and are centered on the cluster center: $\alpha = 201^\circ.69065$, $\delta = -47^\circ.47855$ (Van de Ven et al. 2006).

The first eight plots show the covered areas sorted by month and year, while in the bottom part of Fig. 1 the total coverage of all of the 279 images (on the left), and a zoom of the central part of the cluster (on the right) are shown. In the catalog presented in this work, the proper motion measurements are available only within the field-of-view in common between the two epochs used (see Fig. 1).

3. Photometry, Astrometry, and Calibration

3.1. Photometric reduction

For the reduction of the WFI@2.2m photometric data, we used the software `img2xym.WFI`, a modified version of `img2xym.WFC.09x10` (Anderson & King 2003), which was written originally for *HST* images, adapted successfully to ground-based data, and described in detail in Paper I. We closely followed the prescription given in Paper I for the data reduction of WFI images. This includes standard operations with the pixel data, such as de-biasing, flat-fielding, and correction for cosmic rays hits.

At the basis of the star position and flux measurements, there is the fitting of the *empirical* Point Spread Function (PSF). In our approach, the PSF is represented by a look-up table on a very fine grid. It is well known that the shape of the PSF changes with position in WFI@2.2m chips. This variability can be modeled by an array of PSFs across the chip. The `img2xym.WFI` software works in a fully-automated way to find appropriate stars to represent the PSF adequately. For practical purposes, the number of PSF stars per chip can vary between 1 and 15, depending on the richness of the star-field. An iterative process is designed to work from the brightest to the faintest stars and find their precise position and instrumental flux. A reasonably bright star can be measured with a precision of ~ 0.03 pixel (~ 7 mas) on a single exposure.

Another problem of the WFI@2.2m imager is a large geometric distortion in the focal plane that effectively changes the pixel scale across the field-of-view. There are different ways to map this geometric distortion. We adopted a 9×17 element look-up table of corrections for each chip, derived from multiple, optimally-dithered observations of the Galactic bulge in Baade's Window (Paper I). This look-up table provides the most accurate characterization of geometrical distortions available for the WFI@2.2m. At any given location on the detector, a bilinear interpolation between the four closest grid points on the look-up table provides the corrections for the target point. The derived look-up table may have a lower accuracy at the edges of a field, because of the way in which the self-calibration frames were dithered (see Paper I). An additional source of uncertainty is related to a possible instability distortions in the WFI@2.2m reported earlier. This prompted us to use the local transformation method to derive proper motions (see Sect. 4).

3.2. Sky-concentration correction

Once we obtained star positions and instrumental fluxes for all images, we had to minimize the so-called “sky-concentration” effect. The WFI@2.2m camera is affected significantly by this kind of light contamination (Manfroid & Selman 2001), which is caused by spurious reflections of light at discontinuities in the optics and the subsequent redistribution of light in the focal plane. The insidiousness of the effect is due to the fact that this redistribution of light affects both the science and the flat-field exposures.

Star fluxes are calculated by considering a local sky value, and therefore may be a negligible effect. However, since sky contamination also affects flat images, if it is not corrected properly during pre-reduction procedures, the quantum efficiency of the central pixel will be artificially lower with respect to that of the corner pixel. Consequently, the luminosity of a star measured in the middle of the mosaic camera will be underestimated by ~ 0.1 - 0.2 magnitudes (in V band) with respect to the luminosity of the same star detected close to the mosaic edges.

In Fig. 2a, we plot an instrumental¹ color-magnitude diagram (CMD), which has been zoomed into the horizontal-branch (HB) region of ω Cen, obtained by combining all V and B_{878} images of April 2003. We chose this particular data set to highlight the effect of sky concentration on un dithered images. In fact, this data set has only one pointing, as shown in Fig. 1. The positions of stars on the CCD mosaic is almost identical from one image to

¹ Instrumental magnitudes are calculated to be $-2.5 \times \log(\Sigma_i DN_i)$, where DN are the pixel's Digital Numbers above the local sky summed within a 10-pixel circular aperture. For a mean seeing of $0.8''$, saturation initiates at about ~ -14.5 .

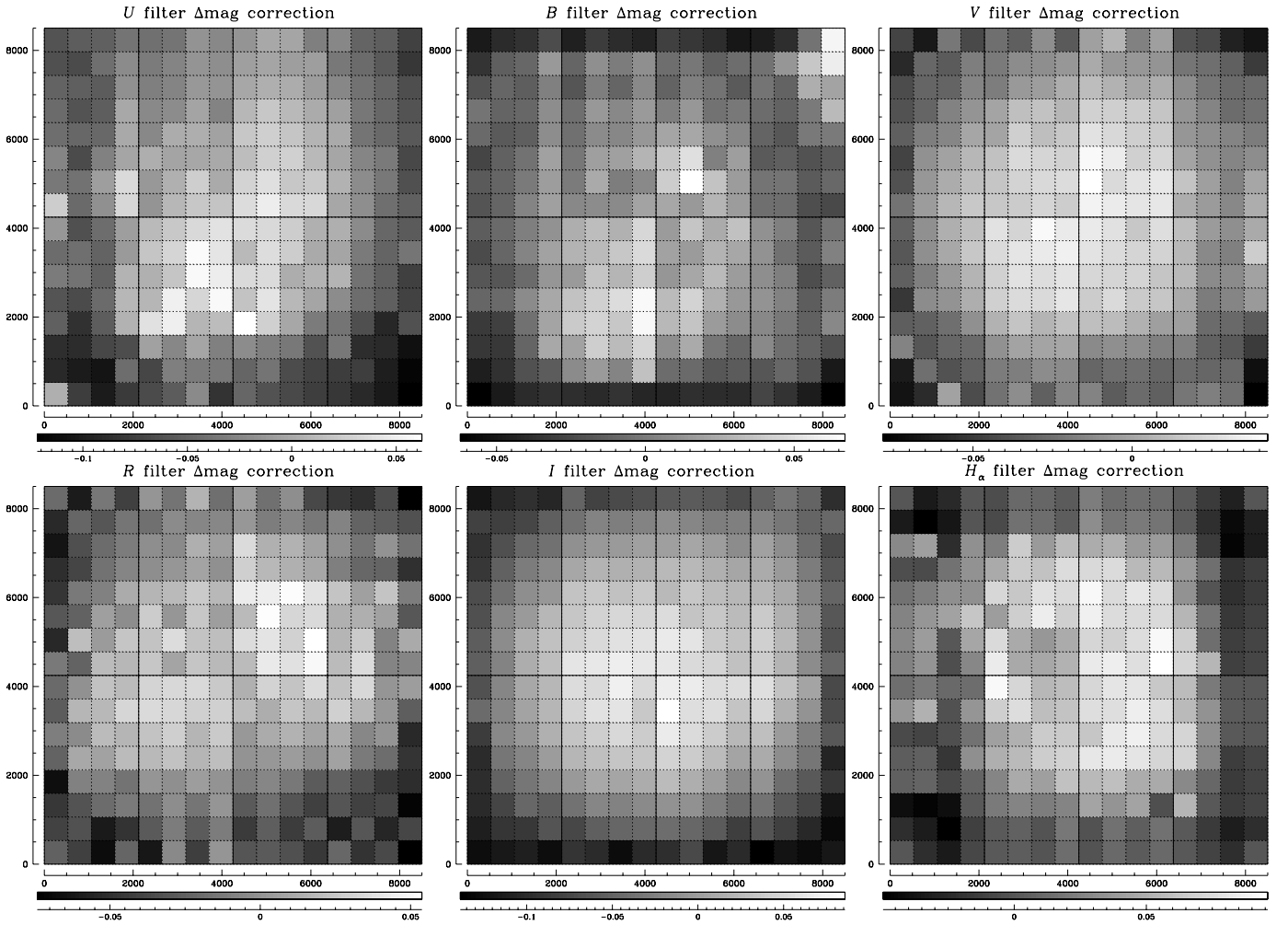


Fig. 3. Final Δmag correction grids for the different filters (B means the B_{842} filter only). Coordinates are in units of WFI pixels. Each WFI chip is highlighted by continuous black lines. Each element of the correction grids is colored according to the corresponding Δmag correction applied. The grey scales are relative to the minimum/maximum correction for each filter.

another, implying a small contribution to the r.m.s of the single star magnitude measurement due to sky-concentration effects. In Fig. 2a, we plotted 1252 stars with $\sigma_V < 0.03$ mag and $\sigma_B < 0.03$ mag, where σ_V and σ_B are the standard errors of a single measurement (r.m.s).

However, with only one pointing, sky concentration maximizes its effect on the relative photometry of stars located at different positions on the image. In Fig. 2a, we highlight the CMD of stars located at different positions on the CCD mosaic: with black dots (994 objects precisely), we show all stars between $2'$ to $6'$ from ω Cen center, which is close to the mosaic center ($x = 4150.69$, $y = 4049.97$ on our master meta-chip). Red points are stars (258 objects) outside $12'$. The displacement of the two HBs clearly shows that sky-concentration effects affect WFI photometry significantly if only one pointing is analyzed, and therefore needs to be corrected.

In our case, the analyzed data sets for different filters come from several pointings (except the case of B_{878} images). In the process of matching all catalogs (for a given filter) to create a single master-frame, the true sky-concentration effect is reduced. For a given star, we considered the mean of the star fluxes originating in different positions and for different pointings, so that the sky-concentration effect in the master frame was reduced.

This process does, however, create systematic errors that affect the global photometry (see Selman 2001).

In Fig. 2b, we show the same zoomed HB region of ω Cen derived, in this case, by matching all the available V and B_{842} images obtained from the ESO archive. This data set contains several different pointings for both filters, so we were able to obtain photometry for the same stars located in some cases close to the mosaic center and in other pointings close to the mosaic edges. All plotted stars have again $\sigma_{B,V} < 0.03$ mag. In this case, only 972 stars (with the same previous convention, 896 black and 76 red) passed the selection criteria on the basis of photometric error. As explained before, matching catalogs for different pointing tends to minimize sky-concentration effects, but without an appropriate correction, r.m.s. of measurements for the stars are enhanced.

Andersen et al. (1995) studied the sky-concentration effect, typical of focal reducers, both by using simulations and analyzing data from the Danish telescope at La Silla. Their method for deriving the sky-concentration correction was based on the complex analysis of many star-field images taken at different orientations and positions during the night. Manfroid et al. (2001) applied a similar method to derive the sky-concentration effect for WFI@2.2m data, while Selman (2001) developed a method to estimate the sky-concentration effect by the analysis of the ze-

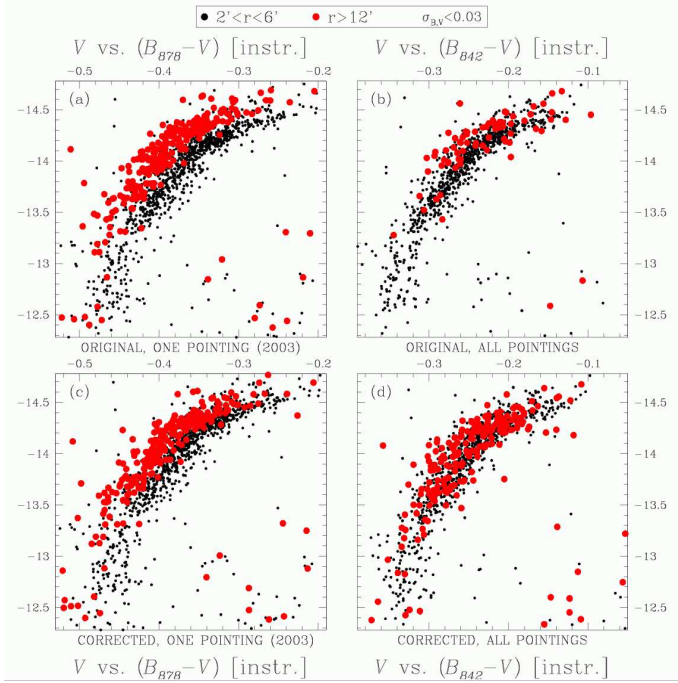


Fig. 2. CMDs zoomed into the HB region of ω Cen. All plotted stars have $\sigma_{B,V} < 0.03$ mag. On the left, we used only images taken in April 2003 (i.e. only one pointing). On the right, we show photometry from all V and all B_{842} images that have independent pointings. Upper diagrams are for the original photometric catalogs. The lower ones are derived from sky-concentration-corrected catalogs. Black dots are stars located close to the mosaic center, while red dots are stars close to the mosaic edges.

ropoint variation in 3 dithered stellar frames, by evaluating this variations using a Chebyshev polynomial fit. They were able to reduce the internal error from 0.034 to 0.009 magnitudes in the V filter, and used the same polynomial fit to correct in addition the photometry in the other filters (see also Selman & Melnick 2005). Koch et al. (2004) provided an analogous prescription to correct for the sky-concentration effect by comparing photometry derived with WFI and Sloan Digital Sky Survey (SDSS) data. Finally, Calamida et al. (2008) used some of the ω Cen images that we present in this work to correct for the positional effects of the WFI camera by means of photometric comparisons with the local standard stars of ω Cen.

The correction given by the ESO team, based on the V filter, consists of a 9th order bidimensional Chebyshev polynomial that should in principle be used also for the U and B filters. Selman (2001) found that his solution for the V band was able to reduce the internal photometric error from 0.029 to 0.010 mag in B , and from 0.040 to 0.014 in U , while for the other filters the V correction failed to reduce the internal photometric error. Selman (2001) argued that this is probably due to problems associated with atmospheric variations affecting data for different filters. Unfortunately, by using the same polynomial coefficients to correct both V and B magnitudes, it is impossible to remove the color degeneracy due to the different response of the CCD to the sky concentration in the two different photometric bands. This degeneracy is of the order of ~ 0.04 - 0.05 mag in color in our V versus $B - V$ CMD between inner stars ($r \sim 4'$) and outer stars ($r > 12'$).

Our adopted solution consists of a self-consistent autocalibration of the sky-concentration map, and takes advantage of the high number of images analyzed, taken with different pointings. Below, we provide a description of the autocalibration procedure. We measured the raw magnitude $\text{mag}_{i,j}$ of each i -star, in each j -image. We selected an image to be a reference frame (at the center of the dither pattern), and by using common stars with frame j we were able to compute the *average* magnitude shifts to bring each image-catalog onto the magnitude reference frame (Δ_j).

If there were no systematic errors, the same stars measured at different positions in two different frames, should have the same magnitude value, within the random measurement errors:

$$\text{mag}_{i,0} - \Delta_0 = \dots = \text{mag}_{i,j} - \Delta_j = \dots = \text{mag}_{i,m} - \Delta_m,$$

where m is the total number of images in that filter, used to perform the autocalibration procedure.

However, the same star closer to the center of the camera is systematically fainter than when it is measured closer to the camera edges. For each star, measured in several different frames, and at different positions on the camera, we can compute an average of the values of the magnitudes in the reference system:

$$\overline{\text{mag}}_i = \left(\frac{1}{m} \right) \sum_{j=1}^m (\text{mag}_{i,j} - \Delta_j).$$

In the same way, we can compute a residual for the i -star in the j -image:

$$\delta_{i,j} = (\text{mag}_{i,j} - \Delta_j) - \overline{\text{mag}}_i.$$

All the residuals of stars close to the center will be systematically positive, and those close to the edges systematically negative. It appears clear that –at any given location on the camera– the average of the residuals from all the stars measured close to that location will provide a first spatial correction to our photometry. It also appears clear that the determination of the sky-concentration photometric correction will be an iterative process.

To guarantee convergence, we applied half of the recommended correction at the given location, to all our image catalogs. We then recomputed the Δ_j , and repeated the procedure until all the residual averages, at any given location, became smaller than 0.001 magnitudes. The null hypothesis of this procedure is that the same star is imaged several times at different locations on the detector. To avoid systematic error, we also select, for each filter, the same number of exposures per different pointing (as much as possible with the existing database).

We use only those stars of the image catalogs with high S/N ratio (i.e. instrumental magnitude from -11 to -14) with a quality PSF-fit smaller than 0.1 (as defined by Anderson et al. 2008), and not too close to the cluster center (which does not necessarily coincide with the center of the camera) to avoid crowding, which compromises the photometric precision. The exact closeness to the center of the cluster depends on the image exposure time; we excluded stars within a radius of 1000-2000 pixels from the ω Cen center.

At this point, we define the expression of “given location”. After several tests, we found a spatial grid of 16×16 boxes to be the most suitable compromise between a large number of residuals ($\delta_{i,j}$) and a spatial resolution of correction sufficiently high to be useful. In Fig. 3, we show our final correction grids, respectively for U , B_{842} , V , R_C , I_C , and H_α filters. For each filter, we present the final 16×16 element correction grid. Each element

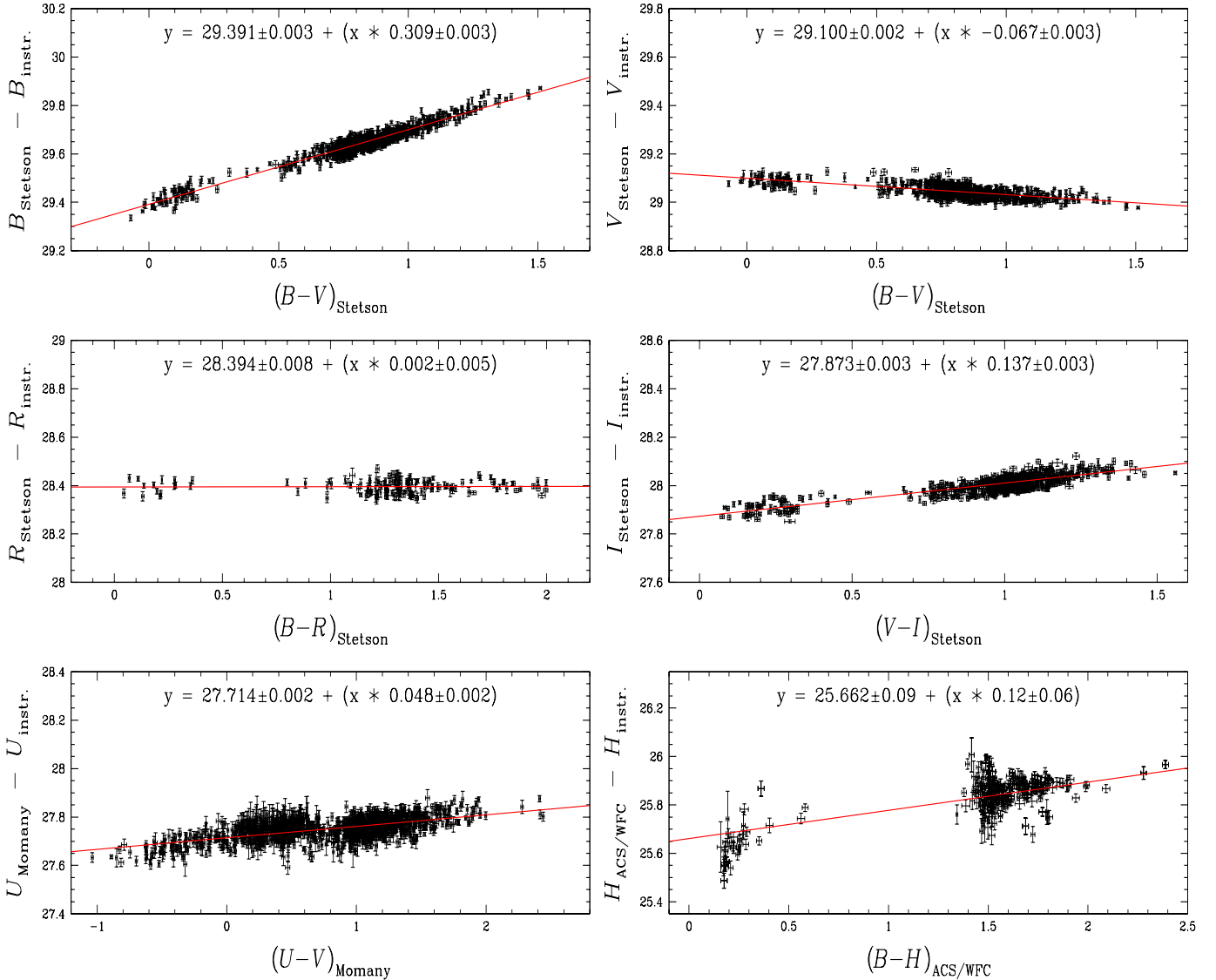


Fig. 4. These figures show our calibration fits with the adopted color equations. For the B , V , R_C , I_C filters we used the on-line set of standard stars provided by Stetson, while for U and H_α bands we used as reference stars the Momany et al. (2003) catalog and the ACS/WFC catalog of Villanova et al. (2007), respectively. See text for more details.

is colored according to the grey scale values (black for the minimum, white for the maximum). The grey scales vary linearly from the minimum to the maximum grid value for each filter. It is clear that sky concentration affects different filters in different ways, and each filter must therefore be corrected independently. To evaluate the correction at any point of the camera, we completed a bilinear interpolation of the closest 4 grid points. The adopted correction was less accurate close to the mosaic edges, where the peripheral grid-points have been stretched toward the boundaries. The available pointings for the other filters are also lower than for B_{842} and V , implying a less effective correction of the sky concentration.

We emphasize that our correction is not completed by a star-to-star comparison. After the spatial correction, a single star cannot have a lower random error (higher precision) than mag_i . However, the systematic errors (accuracy) of single stars relies on the quality of individual grid-point solutions, which were always calculated to be the average of residuals for several stars within each of the 16×16 cells. Even if our random errors for in-

dividual stars are ~ 0.1 mag, with just 10 stars [in the worst case we still have at least 10 such stars] we can reduce our systematic errors to ~ 0.03 mag. The condition that each star has to be observed in each of the 16×16 cells is the ideal case. Deviations from this ideal case occur frequently, although overall, we are close to achieving the optimal solution.

The total amplitude of our correction for the V filter is 0.13 mag. For the same filter, Manfroid & Selman (2001) evaluated a 0.13 mag correction of similar spatial shape. Nevertheless, the two totally independent calibrations appear to be qualitatively the same. Based on the cell-to-cell scatter with the knowledge that sky-concentration is relatively flat, in V and I filters (for which we have more images) we estimate that the accuracy of our solution is as good as ~ 0.03 mag. Although our corrections do not use any color information, we note that the post-corrected CMD is in excellent agreement with (to within a few hundreds of a magnitude) the HB location (Fig. 2).

To verify qualitatively the high quality of our sky-concentration correction procedure, we show in Fig. 2d the same

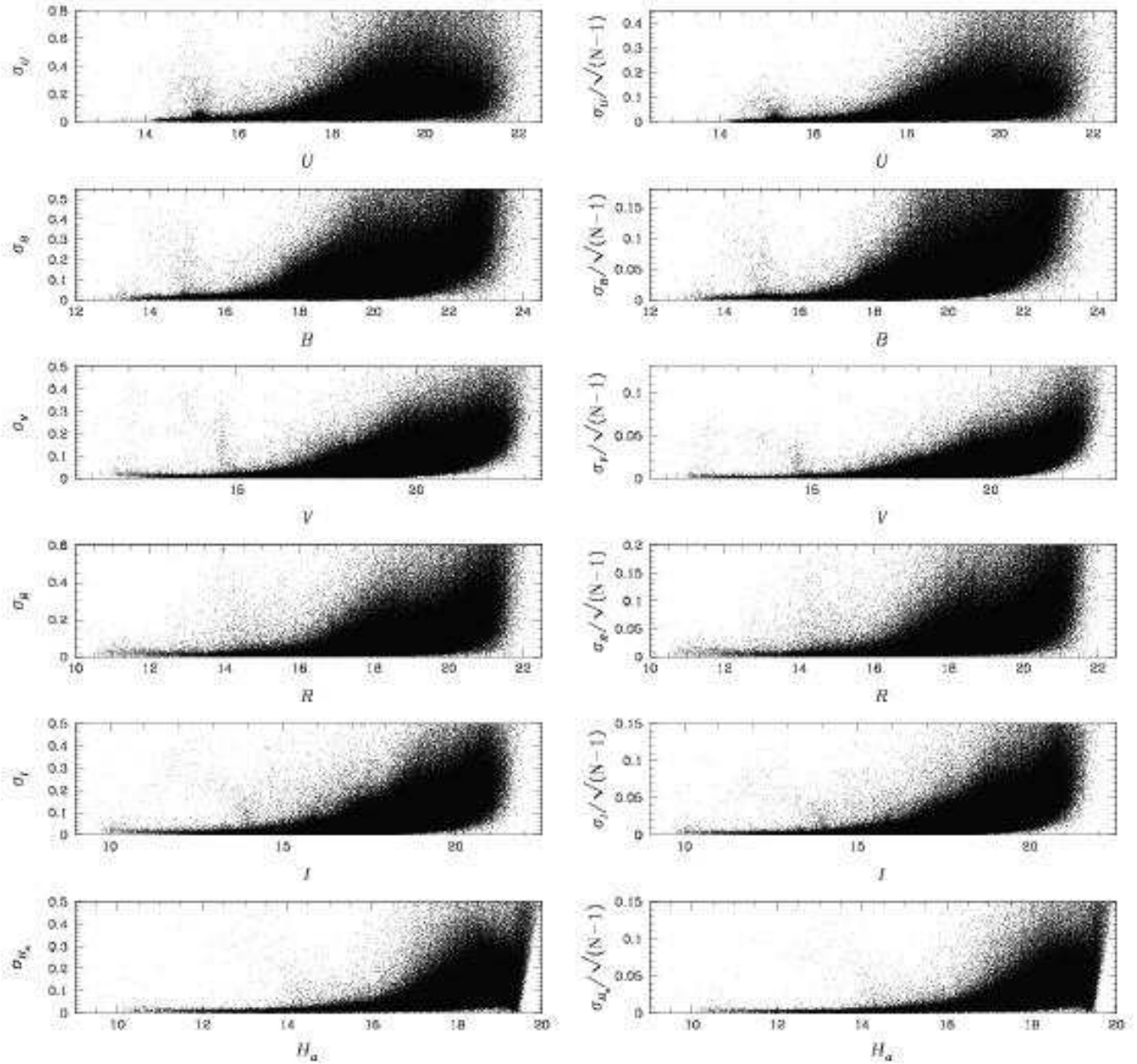


Fig. 5. (*Left panels*): plot of magnitude r.m.s (σ) as a function of magnitude. (*Right panels*): plot of the standard error of the mean ($\sigma/\sqrt{N-1}$, where N is the number of measurements) as a function of magnitude.

CMD region (V vs. $B_{842} - V$), derived using all the available images, after applying our correction. Stars located at different positions on the meta-chip are not affected by the sky-concentration effect, and are located in the same CMD region. The total number of plotted stars (1227, all with $\sigma_{B,V} < 0.03$ mag) is comparable with that of Fig. 2a; this implies that we were able to remove the systematic contribution from our photometric r.m.s values.

Our solution works well for the available ω Cen archive data sets (used to derive the corrections), but archive observations, in general, do not map every chip in a way that enables a sky-concentration correction that is universally applicable to be derived. We cannot guarantee that our solution can be applied to achieve the same positive results with other data sets. As proof

of this issue, we applied our B_{842} solution, to B_{878} images with only one pointing.

Images collected using the B_{842} and B_{878} filters are not so different, in term of central wavelength (see Table 2): sky-concentration effects appear to be similar for almost identical filters (since they are related to atmospheric variations that affect the data for a range of different filters), so a photometric improvement is expected after correcting B_{878} images with our B_{842} -derived solution. If our solution fails to correct the B_{878} photometry, this is probably due to the different pointings of the two B filters instead of the filters themselves. As shown in Fig. 2c, we found that a photometric improvement is present, with respect to Fig. 2a, but that the correction is not satisfactory.

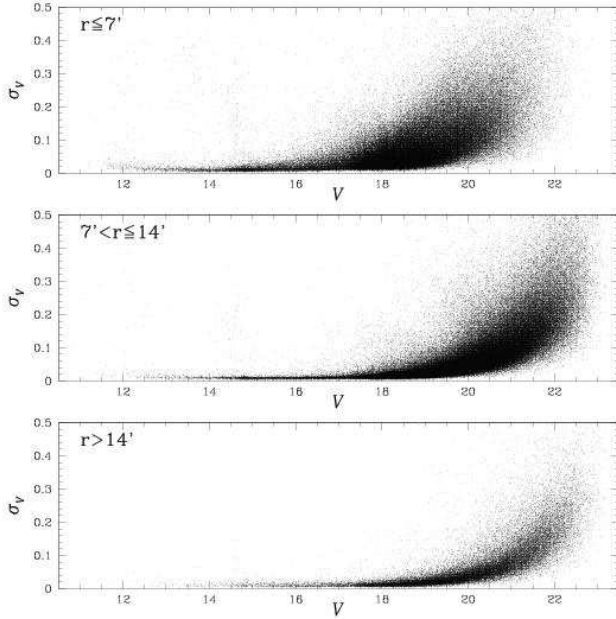


Fig. 6. Photometric r.m.s for stars within $7'$ (top panel), from $7'$ to $14'$ (middle panel), and outside $14'$ (bottom panel).

3.3. Instrumental $UBVR_CI_C$ - H_α photometric catalog

We derived instrumental single-filter catalogs using all available images, by matching each chip individually to minimize the zeropoint differences between WFI chips. Included stars were measured in at least three distinct images. Photometric single-filter catalogs were then linked to the astrometric one. Linked star positions agreed with those in the proper-motion catalog within 1 pixel for $BVR_CI_C H_\alpha$ filters, while for the U filter we had to adopt a larger matching radius (3.5 pixels). This is mainly due to the poorer distortion solution in the U band.

Due to the aforementioned sky-concentration minimization problem with B_{878} images, our B photometry refers to the B_{842} filter.

As for the U photometry, we used only U_{877} images: in fact, U_{841} is a “medium” rather than a wide-band filter, of quite different central wavelength and a low transmission efficiency with respect to U_{877} (Table 2). If not specified otherwise, we refer to B_{842} and U_{877} simply using B and U , respectively.

3.4. Photometric calibration

The photometric calibration of the WFI@2.2m data for BVR_CI_C bands was performed using a set of ~ 3000 online wide field photometric ω Cen Secondary Standards stars (Stetson 2000, 2005). The Secondary Standards star catalog covers an area of about $30' \times 30'$ around the cluster center. We calibrated our U instrumental photometry by cross-correlating our photometry with Momany et al. (2003) U calibrated catalog (Stetson does not provide U photometry for the ω Cen Secondary Standards). For H_α calibration, we used as reference-standard stars the 3×3 central ACS/WFC mosaic photometric catalog in F658N band (GO 9442), which was presented by Villanova et al. (2007). This *HST* catalog was obtained using *img2xym_WFC.09x10* software; instrumental magnitudes were transformed onto the ACS Vega-

mag flight system following Bedin et al. (2005), and by using the zero points of Sirianni et al. (2005).

For BVR_CI_C bands, we matched our instrumental magnitudes and colors to the Stetson standard ones, and derived calibration equations by means of an iterative least squares fitting of a straight line (see Fig. 4). For these filters, we found that only a first-order dependency of the color term affects our instrumental magnitudes. The linearity of our calibration equations, which cover a wide range of colors (being derived from both HB and RGB stars) is evident from the plots of Fig. 4.

As in the calibration of our U instrumental photometry, the Momany et al. (2003) catalog was not corrected for sky-concentration effects. We found a magnitude dependence related to the star positions. We adopted a straight line fit to derive the calibration equation, because we were unable to consider the different color/magnitude dependencies individually. Therefore, our calibrated U magnitudes were not more reliable than the 0.15 magnitude level (maximal error).

For the H_α filter, we again performed a straight line fit to derive the calibration equations, even though the data appear to suggest a second order color effect (see the corresponding panel of Fig. 4). ACS/WFC data cover only the inner $\sim 10' \times 10'$ region of our catalog, and are therefore taken in extremely crowded conditions. This effect might strongly influence our photometry mimicking the aforementioned second-order effect. In Fig. 5, we show in the left panels our photometric errors for each filter, as a function of the corresponding magnitude. The photometric errors (standard deviation) have been computed from multiple observations, all reduced to the common photometric reference frame in the chosen bandpass. In the right panels of Fig. 5, we plot the photometric standard error of the mean –to be defined as $\sigma/\sqrt{N-1}$, where N is the total number of observations– versus the magnitude, for each filter.

To illustrate more clearly the dependence of our photometric r.m.s on crowding, we show (for the V filter only) in Fig. 6 the photometric r.m.s σ_V with respect to V for stars within $7'$ (top panel), from $7'$ to $14'$ (middle panel), and outside $14'$ (bottom panel). Stars located in the most crowded region of the field suffer higher uncertainty in their photometry.

Our final catalog consists of about 360 000 stars, in $UBVR_CI_C$ wide-band and 658nm narrow-band filters, covering a wide area ($\sim 33' \times 33'$) centered on ω Cen. We reach 3 magnitudes in V band below the TO point with a photometric r.m.s of 0.03 mag.

3.5. Zeropoint residuals

Even if our sky-concentration correction works well, residuals are still present, especially close to the corners of our final catalog. Due to the wide field area analyzed in this work, there is also the possibility of a contribution from differential reddening. Using *ubvy* Strömgren and $V I$ photometry, Calamida et al. (2005) developed an empirical method to estimate the differential reddening of ω Cen. The authors found that the reddening can vary in the range $0.03 \leq E(B-V) \leq 0.15$ from Strömgren filters, and $0.06 \leq E(B-V) \leq 0.13$ from $V I$ filters, within their analyzed field-of-view of $14' \times 14'$, which was centered on the center of ω Cen. However, the results by Calamida et al. (2005) were questioned by Villanova et al. (2007), and the quantitative value of the differential reddening still needs to be confirmed.

In the case of the $B-V$ color, the maximum zeropoint residual in our final catalog is less than 0.1 mag. To minimize any zeropoint variations, we used a method similar to that described

by Sarajedini et al. (2007). Briefly, we defined the fiducial ridge-line of the most metal-poor component of the ω Cen RGB and tabulate, at a grid of points across the field, how the observed stars in the vicinity of each grid point may lie systematically to the red or the blue of the fiducial sequence; this systematic color offset is indicative of the local differential reddening.

Our online catalog magnitudes are not corrected for differential reddening to enable the user to adopt their preferred correction method in removing differential reddening and zeropoint residuals.

4. Proper-motion measurements

To complete the proper-motion analysis, we used only the B and V images taken in April 1999 (epoch I) and April 2003 (epoch II). This choice was due to the fact that: (i) we have a fine-tuned geometric distortion correction map for V filter (Paper I), which has been proven to work well for the two B filters (Paper I); (ii) it offers the widest possible time base-line of ~ 4 yrs; and (iii) we have a relatively high number of images in both epochs, and with relatively deep exposures.

We first photometrically selected probable cluster members in the V versus $B - V$ color-magnitude diagram. These stars are located on the RGB (see the RGB selections in the top-panel of Fig. 13, within the magnitude interval $14.6 < V < 17.2$. We used these stars only as a local reference frame to transform the coordinates from one image to the system of the other images at different epochs and therefore derive relative proper motions. By using predominantly cluster stars, we ensure that proper motions will be measured relative to the bulk motion of cluster stars. The expected intrinsic velocity dispersion of ω Cen stars for which we can measure reliable proper motions, is between 10 and 15 km s^{-1} (Merritt, Meylan & Mayor 1997). If we assume a distance of 5.5 kpc for ω Cen, as reported by Del Principe et al. (2006), and isotropic distribution of stars (good to first order), then these translate into an internal dispersion of 0.4-0.6 mas yr^{-1} .

Over the four-year epoch, the difference would result in a displacement of only 1.5-2.3 mas, which is a factor of 3 smaller than the random measurement errors (~ 7 mas). Conversely, the tangential velocity dispersion of field stars is a factor of ~ 10 larger than the intrinsic velocity dispersion of the cluster. For field stars, proper motions are clearly not negligible with respect to measurement errors, and this has an adverse effect on the coordinate transformations. We removed iteratively stars from the preliminary photometric member list that had proper motions clearly inconsistent with cluster membership, even though their colors placed them close to the fiducial cluster sequence.

To minimize the effects of geometric-distortion-solution residuals on proper motions, we used local transformations based on the closest 20 reference stars, typically extending over ~ 30 arcsec. These were well-measured cluster stars of any magnitude selected to be on the same CCD chip, as long as their preliminary proper motion is consistent with cluster membership. No systematic errors larger than our random errors are visible close to the corners or edges of chips.

To avoid possible filter-dependent systematic errors, we measured proper motions in the V and B bandpasses only, for which the geometrical distortion corrections were derived originally (Paper I). Individual errors of proper motions for single stars were estimated as described in Sect. 7.3 of Paper I. For both epochs separately, we estimated the intra-epoch r.m.s error from all same-epoch plates transformed locally to the same reference frame. The proper-motion errors were computed to be the r.m.s of the proper motion, obtained by solving locally each

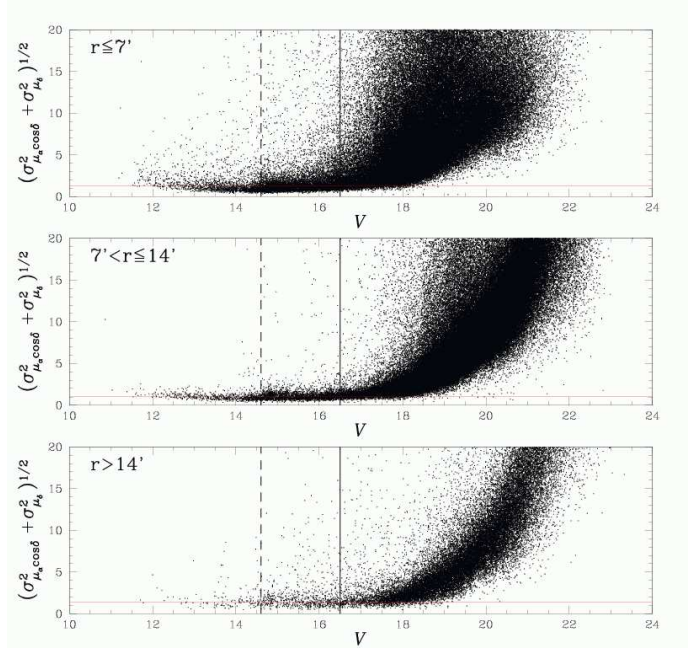


Fig. 7. Proper-motion errors for stars within $7'$ (top panel), from $7'$ to $14'$ (middle panel), and outside $14'$ (bottom panel). The proper-motion errors are expressed in the units of mas yr^{-1} .

first-epoch frame into each second-epoch frame. These errors, however, were not entirely independent because the same frames were used more than once. Therefore, to obtain our most reliable estimate of the proper-motion standard error, we added in quadrature the intra-epoch r.m.s of each epoch.

In Fig. 7, we show our proper-motion r.m.s, in units of mas yr^{-1} , versus V magnitudes, calculated as $\sigma_\mu = \sqrt{\sigma_{\mu_\alpha \cos \delta}^2 + \sigma_{\mu_\delta}^2}$. The top panel presents stars within $7'$ of the center of ω Cen, the middle panel is for stars between $7'$ and $14'$, while the lower panel shows the errors for stars outside $14'$. The vertical dashed line indicates the saturation limit of the deepest exposures ($V = 14.6$), while the continuous line is at $V = 16.5$, the vL00 faintness limit. The precision of our proper-motion measurement is $\lesssim 0.03$ WFI pixels in 4 yrs down to $V \sim 18$ mag (i.e. $\sigma \lesssim 1.9 \text{ mas yr}^{-1}$). At fainter magnitudes, the errors gradually increase, reaching $\sim 5 \text{ mas yr}^{-1}$ at $V = 20$. The stars brighter than $V \sim 13$ magnitude show a higher dispersion because of the image saturation even in the shortest exposures. Horizontal lines in Fig. 7 indicate the median proper-motion r.m.s of unsaturated stars brighter than $V = 16.5$. We have 1.3 mas yr^{-1} , 1.1 mas yr^{-1} , and 1.3 mas yr^{-1} for the top, middle, and bottom panel, respectively. The higher value for the inner stars is due to crowding while, for the outer stars, there is a combination of three factors: (1) our geometrical distortion solution is less accurate close to the WFI mosaic edges; (2) there are fewer cluster members, per unit area, usable as a reference for deriving proper motions; (3) we have a lower number of images that overlap with the external areas of the field-of-view.

4.1. Cluster CMD decontamination

To probe the effectiveness of our proper motions in separating cluster stars from the field stars, we show in Fig. 8 the vector-point diagrams (VPDs, top panels), and the CMDs in the V vs.

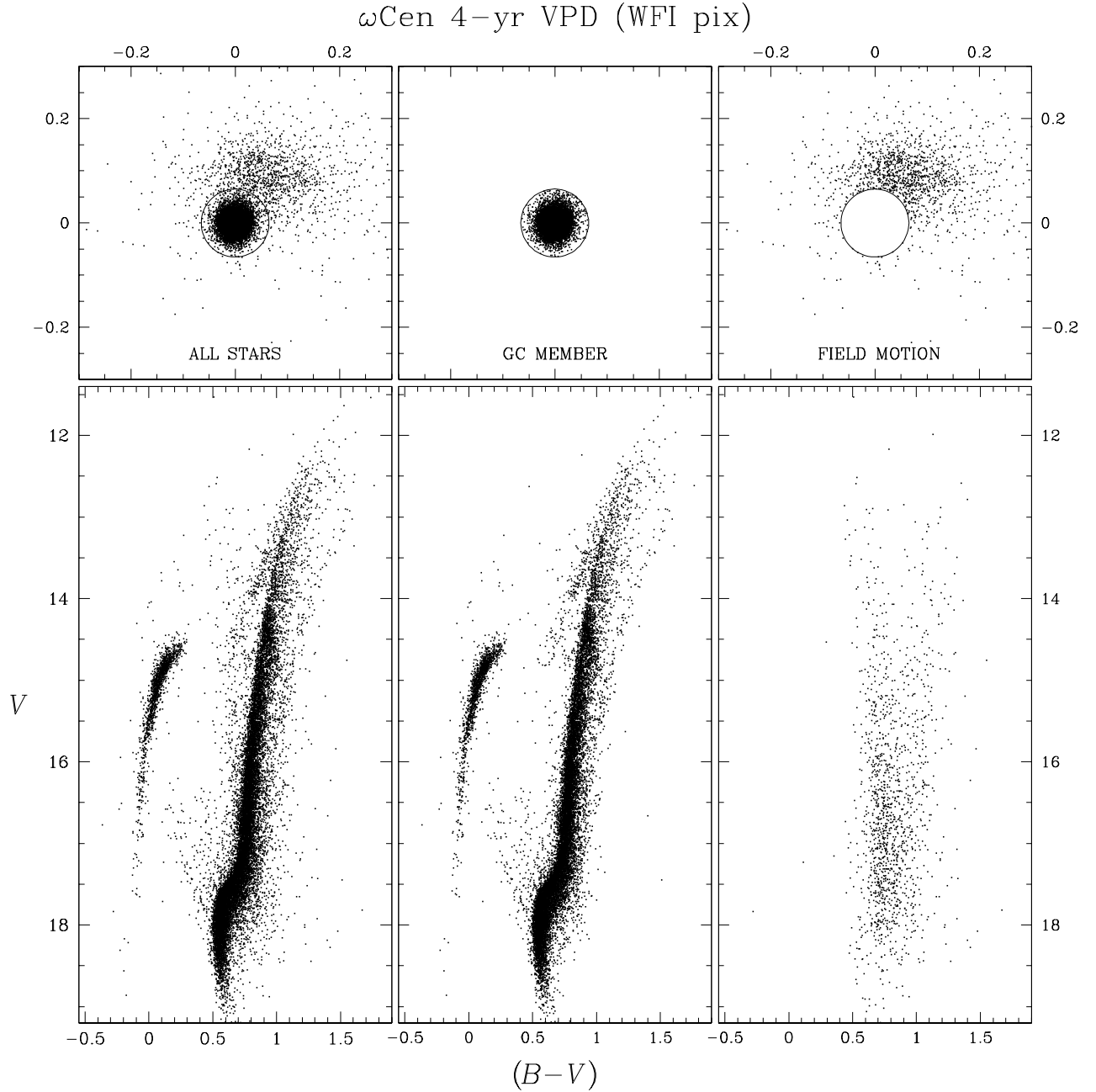


Fig. 8. (*Top-panels*): proper-motion vector-point diagram. Zero point in VPD is the mean motion of cluster stars candidates. (*Bottom panels*): calibrated V , $(B - V)$, color-magnitude diagram. (*Left*): the entire sample. (*Center*): stars in VPD with proper motion within 0.065 pixels (i.e. ~ 3.9 mas yr $^{-1}$) around the cluster mean. (*Right*): probable background/foreground field stars in the area of ω Cen studied in this paper. All plots show only stars with proper-motion σ smaller than 0.032 pixels (i.e. ~ 1.9 mas yr $^{-1}$) and V magnitude r.m.s. smaller than 0.02.

$B - V$ plane (bottom panels). In the left panels, we show the entire sample of stars; the middle panels display what we considered to be probable cluster members; the right panels show predominantly the field stars. Plotted stars have a V r.m.s. lower than 0.03 mag.

In the VPDs, we draw a circle around the cluster centroid of radius 3.9 mas yr $^{-1}$. Provisionally, we define as cluster members all points in the VPD within this circle. The chosen radius is the optimal compromise between missing cluster members with uncertain proper motions, and including field stars that have veloc-

ities equal to the cluster mean proper motion. Even this approximate separation between cluster and field stars demonstrates the power of proper motions derived in this study. A description of membership probability is given in Sect. 5.

4.2. Differential chromatic refraction (DCR)

The DCR effect causes a shift in the photon positions in the CCD, which is proportional to their wavelength, and a function of the zenithal distance: blue photons will occupy a position that

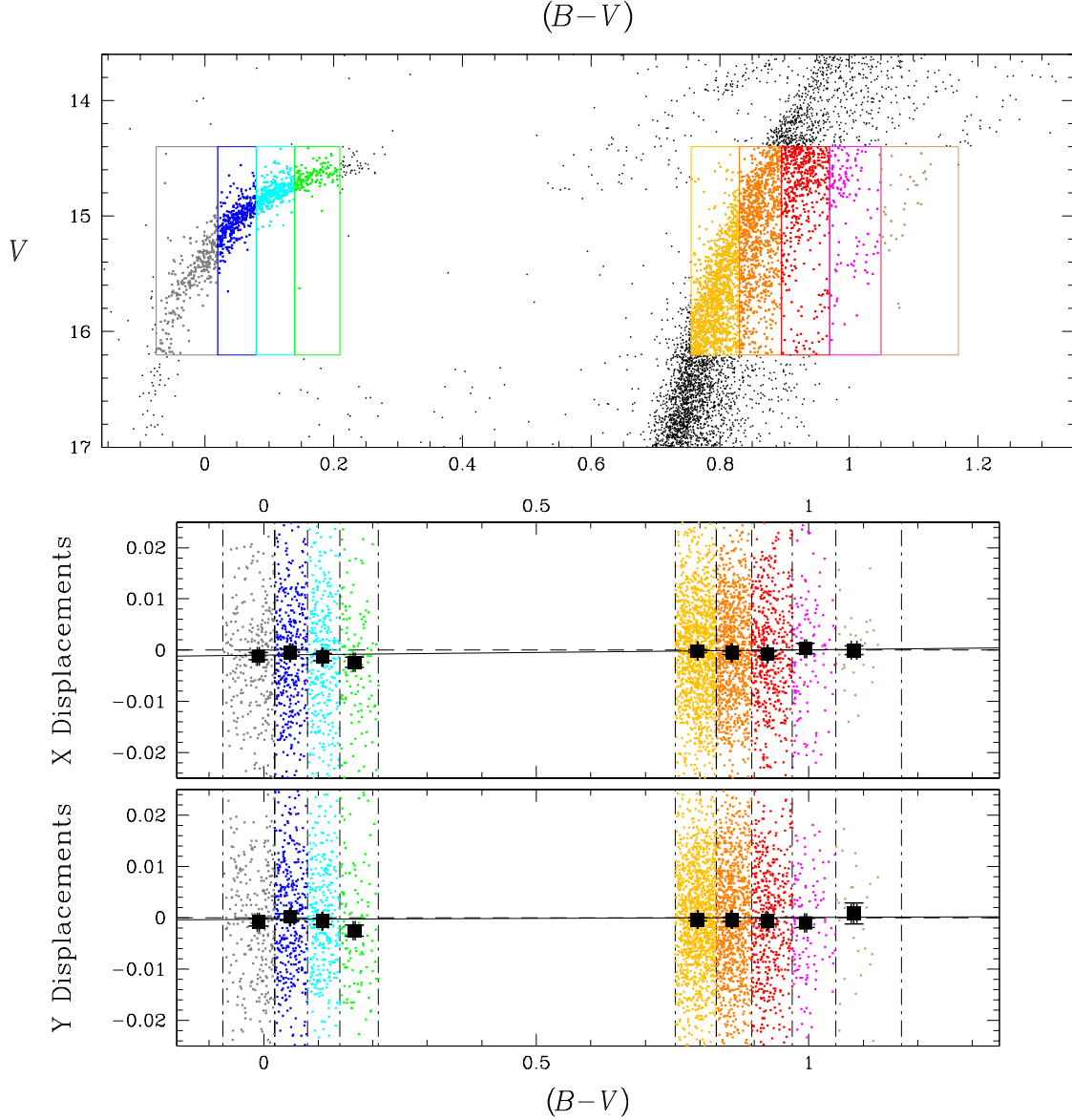


Fig. 9. (*Top panel*): selected stars in the CMD of ω Cen for DCR effect correction. (*Middle and bottom panels*): star displacements along X and Y axes, as a function of stars $(B - V)$ color. The median shift of the nine samples are also showed, with errors. The continuous lines show the adopted fits used to quantify the DCR effects.

differs from that of red photons. The DCR effect is easier to detect and remove from CCDs, due to their linearity.

Unfortunately, within each epoch, the available data sets are not optimized to perform the DCR correction directly (Monet et al. 1992), because the images have not been taken at independent zenithal distances. We can, however, check if possible differences in the DCR effect between the two epochs could generate an apparent proper motion for blue stars relative to red stars.

We selected four samples of stars located on the HB, and five on the RGB, as shown in Fig. 9 (top panel), with different colors to estimate the DCR effect, in a magnitude interval of 1.8 mag in V ($14.4 \leq V \leq 16.2$), with proper motions $\leq 3.8 \text{ mas yr}^{-1}$ and r.m.s. $\leq 1.9 \text{ mas yr}^{-1}$. We chose this magnitude range to: (i) avoid luminosity-dependent displacements (if any); (ii) include

stars with a low r.m.s. in positions and fluxes (see Fig. 5, 7), excluding saturated stars; and (iii) cover the widest possible color baseline according to the above points (i) and (ii). For each of the nine samples, we derived the median color and the median proper motion along $\mu_\alpha \cos \delta$ and μ_δ , and their respective errors. Proper motions were expressed in the terms of a displacement over 4 years, that is in the units of WFI pixels along the X and Y axes of a detector (parallel to the RA and Dec directions).

In Fig. 9, we show, in the top panel, the selected stars on the CMD used to examine the DCR effect; the linear fits adopted for the X and Y displacements are shown in the lower part of the figure. We found a negligible DCR effect along both X and Y axes. For this reason, we have not corrected our measurements for this effect.

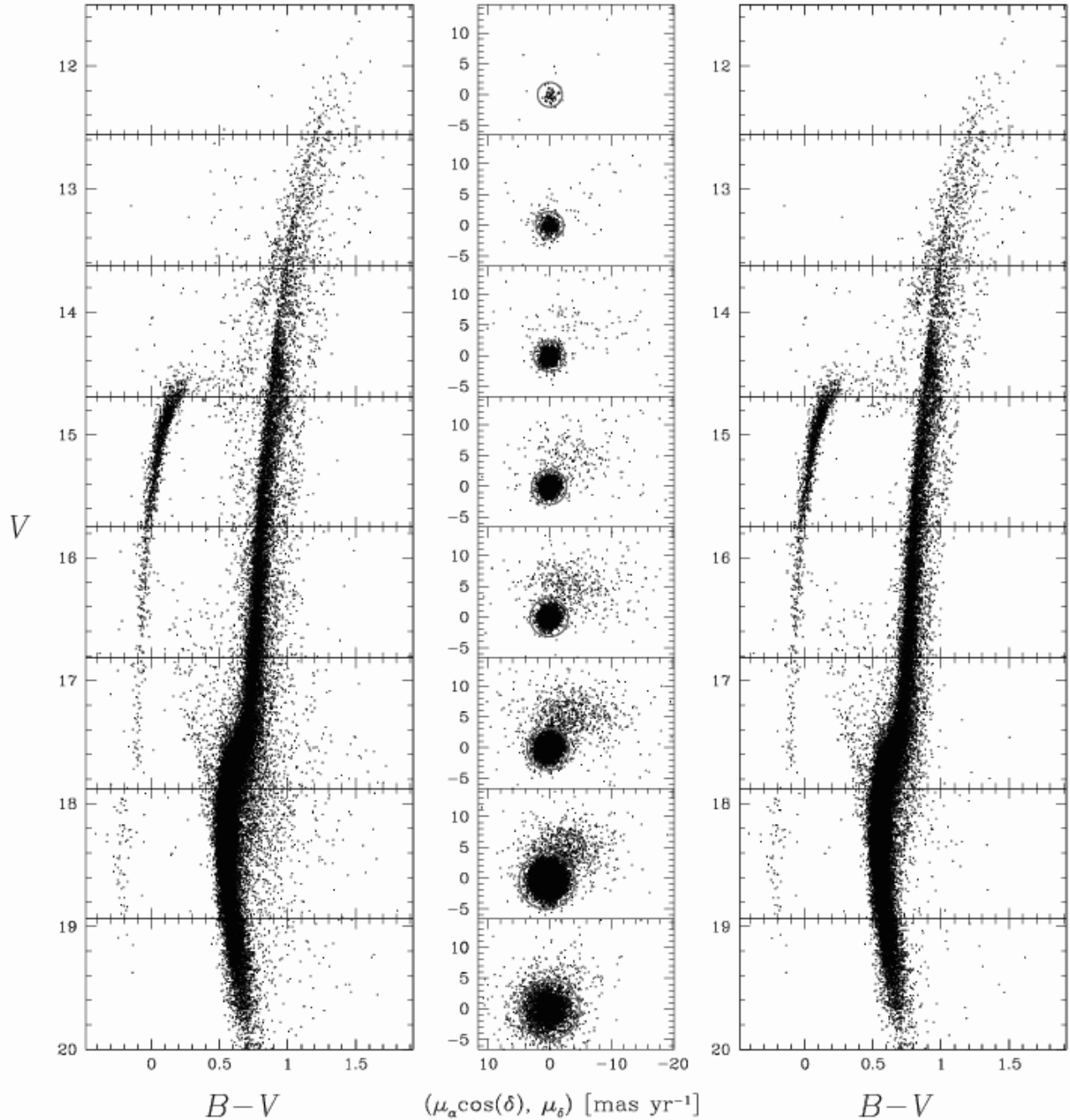


Fig. 10. (Left): color-magnitude diagram, splitted into eight magnitude bins, for all the stars having a proper-motion r.m.s. increasing from 1.8 mas yr^{-1} for the brightest bin to 5 mas yr^{-1} for the faintest one, and photometric r.m.s. from 0.02 mag to 0.05 mag , generous enough to include main sequence stars down to $V = 20$. (Middle): proper motions for the stars in the corresponding magnitude intervals. A circle in each diagram shows the adopted membership criterion. (Right): color-magnitude diagram for assumed cluster members.

In Fig. 10, we show, on the left, our calibrated V , $B-V$ CMD, divided into eight magnitude bins. In each bin, we adopted different selection criteria to identify cluster members, which were more stringent for stars with more reliable measurements from data of high signal-to-noise ratio, and less restrictive for star with less precise measurements. Plotted stars have a proper-motion r.m.s. of $< 1.8 \text{ mas yr}^{-1}$ for the brightest bin, to 5 mas yr^{-1} for the faintest one. The Photometric r.m.s. for both the bands range between 0.02 mag for the brightest bin to 0.05 for the faintest

one, which is sufficient to include main-sequence stars down to $V = 20$. For each magnitude bin, we considered as cluster members those stars with a proper motion within the circle shown in the middle column of Fig. 10.

On the right side of Fig. 10, we show the color-magnitude diagram for stars assumed to be cluster members. The available archive images are again not sufficiently deep to derive reliable proper motions below the TO. The proper motions presented in this paper are not sufficiently accurate to study the internal mo-

tion of ω Cen. The main purpose of the proper motion presented in this work is to provide a reliable membership probability for spectroscopic follow-up projects, star counts, and the study of the radial distribution of the different branches (Bellini et al. in preparation).

4.3. Astrometric calibration

To translate the pixel coordinates into the equatorial coordinate system, we adopted the UCAC2 catalog (Zacharias et al. 2004) as a reference frame. Due to the severe crowding in images of the inner parts of ω Cen, this catalog was however inadequate for calibration purposes close to the center of ω Cen (the central $10' \times 10'$ area corresponds almost entirely to a void in UCAC2). Another possible reference frame, especially for the cluster center, is the vL00 catalog. However, the precision of published coordinates is lower than ~ 20 mas and no analysis was provided by vL00 for the presence of potential systematic errors in the positions. Examination of vL00 proper motions by Platais et al. (2003) indicated that *a priori* these systematic errors could not be discounted. These deficiencies in the vL00 positional catalog were eliminated by re-reducing the original Cartesian coordinates (of formal precision equal to 2 mas), kindly provided by F. van Leeuwen.

First, we selected only Class 0-1 stars from vL00 (i.e. their images were isolated or only slightly disturbed by an adjacent image). Second, a trial equatorial solution was obtained for vL00 stars using the UCAC2 catalog as a reference frame. Third, the new set of vL00 coordinates was tested against the UCAC2 positions as a function of coordinates, magnitude, and color of stars. There are ~ 3000 stars in common between these two sets of coordinates. Assuming that the UCAC2 positions are free of magnitude- color-related systematic errors, we found that the original vL00 Cartesian coordinates were biased by up to 16 mas mag^{-1} . There is also a detectable quadratic color-dependent bias along the declination. Both magnitude- and color-related biases were removed from the vL00 Cartesian coordinates before the final equatorial solution was obtained.

The new reference catalog, covering a region of $1.5^\circ \times 1.5^\circ$ and magnitudes to $V \sim 16.5$, contains 10 291 stars and consists of approximately equal parts of the UCAC2 (trimmed down to stars with positional accuracies of higher quality than 75 mas) and the updated vL00 coordinates on the system of ICRS and epoch J2000.0.

This new reference catalog was used to obtain the equatorial coordinates of our ω Cen stars. The WFI pixel coordinates of these stars were translated into global Cartesian system coordinates and corrected for geometric distortions. A simple low-term-dominated plate model was sufficient to calculate equatorial coordinates. The standard error of this solution, employing ~ 5500 reference stars, was 45-50 mas in each coordinate. These errors were higher than those listed in Yadav et al. (2008, Paper II), which is based on similar WFI@2.2m data for the open cluster M67. We understand that image crowding remains a dominant source of increased scatter in our solution for ω Cen. Although we removed all stars with obviously poor astrometry, even a close but not overlapping image might slightly distort the position of a star, especially in photographic plates. The J2000 positions of all stars for the epoch 2003.29 are given in Table 6.

The proper motions in this work have not been translated into the absolute values, because there are too few background galaxies suitable for defining an absolute reference frame.

4.4. Comparison with other ω Cen proper-motion catalogs

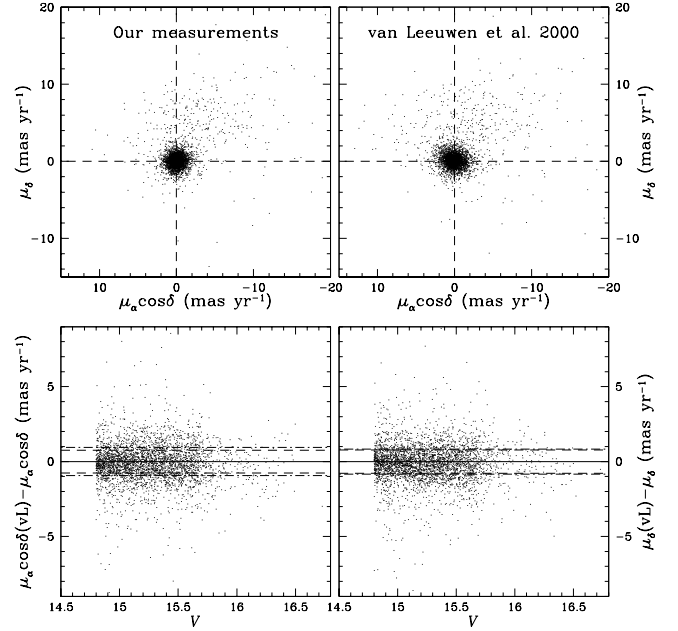


Fig. 11. (Top panels): vector-point diagrams of common stars in our catalog (left) and those of vL00 (right), with respect to the mean cluster motion. (Bottom panels): right ascension (left) and declination (right) proper-motion residuals as a function of the V magnitudes. Horizontal dashed and point-dashed lines show the 3σ -clipped median of the proper-motion dispersion for the selected cluster members, for our measurements and for vL00, respectively.

We compare our results with the proper-motion catalog by van Leeuwen (2000). First, we considered the common, unsaturated stars in our catalog ($V > 14.6$) to the vL00 faint limit ($V \sim 16.5$). The selected samples contained ~ 3400 stars. Since vL00 proper motions are given in an absolute reference system, we subtracted from the individual vL00 proper motions the absolute mean motion of the cluster provided by the same authors [$(\mu_\alpha \cos \delta, \mu_\delta) = (-3.97, -4.38) \text{ mas yr}^{-1}$].

In the top panels of Fig. 11, we show on the left the vector-point diagram from our measurements, while on the right we show the vL00 values. In both diagrams, a concentration of stars at $(0,0) \text{ mas yr}^{-1}$ corresponds to the cluster members, while a diffuse distribution of stars around $(-3, 5) \text{ mas yr}^{-1}$, consists of the field objects in the foreground and possibly the background of ω Cen.

The size of the proper-motion dispersions of the cluster members reflect both internal motions in the cluster and random errors. However, the internal motions are expected to be negligible. Assuming a distance of 5.5 kpc, and the Meylan et al. (1995) measurement of the dispersion in the transverse velocity of $\sim 10 \text{ km s}^{-1}$ (in the outskirts of the cluster that we are probing) the expected dispersion in the proper motions would be $\sim 0.4 \text{ mas yr}^{-1}$. Our estimated errors for the selected sample was 0.74 mas yr^{-1} for $\mu_\alpha \cos \delta$, and 0.77 mas yr^{-1} for μ_δ . Therefore, the internal proper motions should not affect more than 10-15% of the observed dispersions.

To estimate the observed proper-motion dispersion in the two samples (this paper and vL00), we adopted the 68.27-th percentile of the distribution (σ) about the median (estimated iteratively with a 3σ -clipping), and for each coordinate independently. Due to the significance differences between cluster and field object motion, this procedure allowed us to isolate a sub sample of members.

Our results were:

$$\text{this work : } \begin{cases} \sigma(\mu_\alpha \cos \delta) = 0.76 \text{ mas yr}^{-1} \\ \sigma(\mu_\delta) = 0.78 \text{ mas yr}^{-1} \end{cases}$$

$$\text{vL00 : } \begin{cases} \sigma(\mu_\alpha \cos \delta) = 0.94 \text{ mas yr}^{-1} \\ \sigma(\mu_\delta) = 0.83 \text{ mas yr}^{-1} \end{cases}$$

For the selected sample, it is clear that our distribution is tighter, rounder, and in good agreement with our estimate of the errors. Even if our proper motions originate in images representing half the total number of plates used by vL00, we note that we study more than 3 mag fainter in V , and use a time baseline that equals only $\sim 1/12$ of that used by vL00.

The above performed test could be a bit unfair versus the vL00 catalog, because we used our non-saturated stars only, which are the faintest in the vL00 catalog. vL00 demonstrated emphatically that not all stars are suitable for astrometric measurements. We therefore performed a second test in which we chose the stars in vL00 with the most reliable measurements (belonging to class 0 and 1 only) that were brighter than $V = 16$, and had a good probability of being a cluster member ($P_\mu(\text{vL00}) > 75\%$); we compared the measurements for these stars with those in catalog.

The results were as follows:

$$\text{this work : } \begin{cases} \sigma(\mu_\alpha \cos \delta) = 0.68 \text{ mas yr}^{-1} \\ \sigma(\mu_\delta) = 0.69 \text{ mas yr}^{-1} \end{cases}$$

$$\text{vL00 : } \begin{cases} \sigma(\mu_\alpha \cos \delta) = 0.71 \text{ mas yr}^{-1} \\ \sigma(\mu_\delta) = 0.62 \text{ mas yr}^{-1} \end{cases}$$

These results illustrate the slightly higher precision of the vL00 catalog, but the dispersions in the measurements are, in any cases, comparable. The dispersion obtained with our catalog, which now also includes saturated star measurements, is more reliable than found with the first test. The explanation of this apparent paradox is that, by selecting the best proper-motion measured stars in the vL00 catalog (class 0 and 1, among the most isolated stars), we also selected the most isolated stars in our catalog, making the PSF-wings fitting more effective. Once again, it appears clear the huge potential that wide field CCD imager will have in astrometry in the future.

5. Membership probability

In the vector-point diagrams of Figs. 8 and 10, two distinct groups of stars are clearly detectable: the bulk of stars belong to ω Cen, with no mean motion ($\mu_\alpha \cos \delta = \mu_\delta = 0.0 \text{ mas yr}^{-1}$), and there is a secondary broad group, which corresponds to field stars.

Vasilevskis et al. (1958) were the first to formulate the proper-motion membership probability. This method was later developed by many authors (Sanders 1971, Zhao & He 1990, Tian et al. 1998, Balaguer-Núñez et al. 1998, and references therein) for several open and globular clusters. To derive our membership probability, we followed a method based on proper motions described by Balaguer-Núñez et al. (1998).

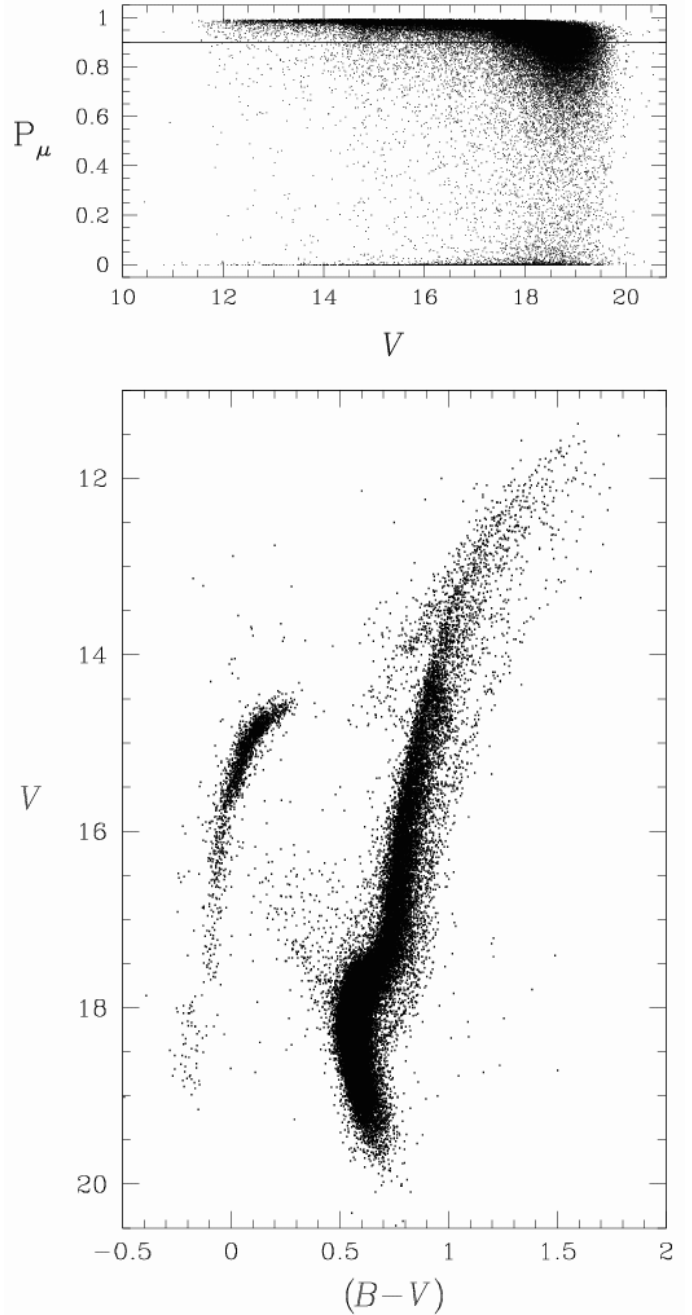


Fig. 12. Membership probability P_μ versus V magnitude for stars with $\sigma_{V,B} < 0.05$ mag and proper-motion r.m.s $< 5 \text{ mas yr}^{-1}$. Horizontal line show the $P_\mu = 90\%$ level. The resulting CMD for stars with $P_\mu > 90\%$ is shown on the bottom panel.

First of all, we constructed frequency functions for both cluster and field stars, Φ_c^v and Φ_f^v respectively, derived from the cluster and field star distribution in the VPD. For the i^{th} star, these functions were as follows:

$$\Phi_c^v = \frac{\exp \left\{ -\frac{1}{2} \left[\frac{(\mu_{x_i} - \mu_{x_c})^2}{\sigma_{x_c}^2 + \epsilon_{x_i}^2} + \frac{(\mu_{y_i} - \mu_{y_c})^2}{\sigma_{y_c}^2 + \epsilon_{y_i}^2} \right] \right\}}{2\pi(\sigma_{x_c}^2 + \epsilon_{x_i}^2)^{1/2}(\sigma_{y_c}^2 + \epsilon_{y_i}^2)^{1/2}},$$

and

$$\Phi_f^v = \frac{\exp \left\{ -\frac{1}{2(1-\gamma^2)} \cdot \left[\frac{(\mu_{x_i} - \mu_{x_f})^2}{\sigma_{x_f}^2 + \epsilon_{x_i}^2} - \frac{2\gamma(\mu_{x_i} - \mu_{x_f})(\mu_{y_i} - \mu_{y_f})}{(\sigma_{x_f}^2 + \epsilon_{x_i}^2)^{1/2}(\sigma_{y_f}^2 + \epsilon_{y_i}^2)^{1/2}} + \frac{(\mu_{y_i} - \mu_{y_f})^2}{\sigma_{y_f}^2 + \epsilon_{y_i}^2} \right] \right\}}{2\pi(1-\gamma^2)^{1/2}(\sigma_{x_f}^2 + \epsilon_{x_i}^2)^{1/2}(\sigma_{y_f}^2 + \epsilon_{y_i}^2)^{1/2}};$$

where (μ_{x_i}, μ_{y_i}) are the i^{th} star proper motions along the X and Y axes, $(\epsilon_{x_i}, \epsilon_{y_i})$ represent the respective displacement r.m.s., (μ_{x_f}, μ_{y_f}) and (μ_{x_c}, μ_{y_c}) are the central points of the field and cluster star proper motion, $(\sigma_{x_f}, \sigma_{y_f})$ and $(\sigma_{x_c}, \sigma_{y_c})$ are the field and cluster star proper-motion intrinsic dispersion, and γ is the correlation coefficient, calculated to be

$$\gamma = \frac{(\mu_{x_i} - \mu_{x_f})(\mu_{y_i} - \mu_{y_f})}{\sigma_{x_f} \sigma_{y_f}}.$$

The spatial distribution was ignored due to the relatively small size of our field ($\sim 33' \times 33'$) with respect to the ω Cen radial extent of $r_t \simeq 57'$ (Harris et al. 1996). For our calculations, we considered only stars with an r.m.s. in proper motion $< 1.9 \text{ mas yr}^{-1}$ to define Φ_c^v and Φ_f^v . The center of the proper-motion distribution in the VPD for cluster stars was found to be at $x_c = 0.00 \text{ mas yr}^{-1}$, and $y_c = 0.00 \text{ mas yr}^{-1}$, with r.m.s. values of $\sigma_{x_c} = 0.83 \text{ mas yr}^{-1}$, and $\sigma_{y_c} = 0.83 \text{ mas yr}^{-1}$. For field stars, we have: $x_f = -3.57 \text{ mas yr}^{-1}$, $y_f = 5.12 \text{ mas yr}^{-1}$, $\sigma_{x_f} = 5.06 \text{ mas yr}^{-1}$, and $\sigma_{y_f} = 2.86 \text{ mas yr}^{-1}$, respectively.

The distribution function for all the stars can be computed as follows:

$$\Phi = (n_c \cdot \Phi_c^v) + (n_f \cdot \Phi_f^v) = \Phi_c + \Phi_f;$$

where n_c and n_f are the normalized number of stars for cluster and field ($n_c + n_f = 1$). Therefore, for the i^{th} star the resulting membership probability is

$$P_\mu(i) = \frac{\Phi_c(i)}{\Phi(i)}.$$

In Fig. 12, we show in the upper panel the P_μ distribution versus V magnitude. To include also faint stars and reach $V = 20$, plotted stars have proper-motion r.m.s. $< 5 \text{ mas yr}^{-1}$ and $\sigma_{V,B} < 0.05 \text{ mag}$. The horizontal line marks the 90% probability level. The lower panel contains the CMD for stars with $P_\mu > 90\%$.

When calculating formal membership probabilities for ω Cen, we have a paradoxical situation in which the main concern is to assign a reasonable probability to field stars. This is because in our sample the number of cluster stars is significantly higher than the small number of field stars. In addition, proper-motion errors have a strong dependence on magnitude (Figs. 7, 10), which is not accounted for in our membership probability P_μ calculation. We therefore, also used the so-called local sample method (e. g., Paper II) for membership probability calculation. In this method, for each target star a sub-sample of stars was selected to reflect closely the properties of a target. This assures a smooth transition in the calculated P_μ as a function of the chosen parameter. For ω Cen, the obvious choice of parameter was the mean error σ_μ of the proper motions. Given the wide range of σ_μ , we chose to consider only stars with $\sigma_\mu < 7 \text{ mas yr}^{-1}$. Less accurate proper motions are marginally useful for membership studies. We note that σ_μ is calculated in the same way as in Sect. 4 and Fig. 9.

For each target star, we then selected a star a subsample of 3000 stars almost with identical proper-motion errors to that of a target star. The trial calculations indicated that we cannot model the distribution of field stars with a Gaussian because the number

of potential field stars in the vector-point diagram is extremely low in the vicinity of the cluster-star centroid (Fig. 11). A reasonable alternative to a Gaussian is a flat distribution of field stars.

In essence, the membership probability P_μ is driven by the distribution of cluster stars. If the modulus of the proper-motion vector of a star exceeds $2.5\text{--}3\sigma_\mu$, the corresponding P_μ is less than 1%. We provide these alternative estimates of P_μ (called $P_\mu(2)$, to distinguish this from the first mentioned method $P_\mu(1)$) for 120 259 stars. For the majority of stars, both values of P_μ are similar. However, there are a number of cases in which the P_μ estimates for the two methods differ radically. In the case of high proper-motion errors for cluster stars, the local sample method clearly provides a more realistic membership probability. A closer inspection of these cases indicates indirectly a potential problem in calculating the proper motion. If the error of proper motion along one axis is several times larger than the error along the other axis, or if this error is too high for a particular magnitude, the chances are that our proper-motion value is corrupted and, hence, its formal membership probability is meaningless.

Unless specified otherwise, we mean $P_\mu(1)$ determination when referring to P_μ .

6. Applications

Our ω Cen proper-motion catalog can be used for different purposes. The first application was the selection of the most probable ω Cen members for spectroscopic follow-up studies. In Villanova et al. (2007), we used the proper-motion catalog of the present paper to pre-select sub-giant branch stars. This helped us to avoid the Galactic field stars close to the TO level. All resultant radial velocities were close to the ω Cen mean value, which confirmed their membership. On the other hand, the high photometric quality and the availability of several filters covering a wide area around the cluster, imply that this catalog is an excellent photometric reference frame on which to register photometry from different telescopes and cameras (Bellini et al. in preparation).

Besides these obvious applications, our ω Cen proper-motion catalog also provides an observational constraint of the origin of the composite stellar populations in ω Cen. Our catalog provides the necessary wide-field coverage and photometric accuracy to investigate the radial distribution of the different ω Cen sub-population from the center of the cluster to $\sim 22'$ (in the corners). We will report on this analysis in a subsequent paper (Bellini et al. in preparation).

6.1. The proper motion of the RGB sub-populations

Ferraro et al. (2002) cross-correlated the WFI photometric catalog of Pancino et al. (2000) with the vL00 photographic proper-motion catalog. Their goal was to investigate the nature of the anomalous metal-rich RGB of ω Cen, the so-called RGB-a. In particular, they investigated the presence of proper-motion mean differences between the ω Cen bulk population (metal-poor RGB, so-called RGB-MP) and the minor, but yet important, metal-rich RGB-a population (Pancino et al. 2000). Their Fig. 2 showed significant variation in the relative proper motion of RGB-a stars with respect to ω Cen RGB-MP motion. In particular, they found that the RGB-a stars had a mean proper motion of $|\delta\mu_{\text{tot}}| = 0.8 \text{ mas yr}^{-1}$ that is offset from that of the RGB-MP population. Therefore, they concluded that the RGB-a

subpopulation must have had an independent origin with respect to the RGB-MP one.

Unsurprisingly, the Ferraro et al. (2002) study triggered new interest in the ω Cen proper motion, and Platais et al. (2003) presented a detailed reanalysis of the vL00 catalog. Platais et al. (2003) concluded that the reported proper-motion offset between the ω Cen sub-populations could be attributed to instrumental bias. However, Hughes et al. (2004) commented that there was no residual color term in the ω Cen proper motions, and that these authors misinterpreted the observed offsets. Specifically, Hughes et al. (2004) asserted that the summary effect of color terms (before the corrections) amounted to no more than $1 \text{ mas yr}^{-1} \text{ mag}^{-1}$ in $B - V$, while the offset in the proper motions for the anomalous ω Cen stars reached 2 mas yr^{-1} and did not have the same direction as the color term. Regardless of the reason for the reported offset in the vL00 catalog, the presence of this offset was not confirmed by the new *HST*-based preliminary proper motions (Anderson 2003).

Two spectroscopic studies completed by Pancino et al. (2007) and Johnson et al. (2008) indicated that there was no evidence for any of the RGB stellar populations to have an offset in the mean radial velocity, or a different radial velocity dispersion. This result applied also to the RGB-a sub-population.

Our astrometric catalog provided an independent data set with which we could test the Ferraro et al. (2002) conclusions. We repeated the same analysis performed in Ferraro et al. (2002). First, we divided the ω Cen RGB population into three subpopulations (see top panel of Fig. 13): RGB-MP (cyan), RGB-a (red), and RGB-Mint (RGB stars between RGB-MP and RGB-a, green). All plotted stars had high membership probability ($P_\mu > 90\%$), and photometric errors ranging from 0.02 mag for bright stars to 0.05 mag for faintest ones, in both filters.

The RGB samples include all stars with $V \leq 17.2$. MP and Mint RGB stars merge with each other at fainter magnitudes. Sollima et al. (2005) and Villanova et al. (2007) clearly showed that the SGB region of ω Cen includes five subpopulations (see again Fig. 15). Three of these merge into each other and form the RGB-MP and RGB-Mint samples. We emphasize that our population sub-division extends to fainter magnitudes than in Ferraro et al. (2002), and therefore provides a higher RGB sampling and more robust statistics. Our samples contain 5182 RGB-MP stars, 3127 RGB-Mint stars, and 313 RGB-a stars.

A closer look at the three RGB sub-population proper motions is presented in the bottom panels of Fig. 13: RGB-MP on the left, RGB-Mint in the middle, and RGB-a on the right. The red crosses report the median value (estimated iteratively) of the proper motion of the three sub-samples. For the RGB-MP sample, we have:

$$\begin{cases} \langle \mu_\alpha \cos \delta \rangle = (0.00 \pm 0.01) \text{ mas yr}^{-1} \\ \langle \mu_\delta \rangle = (-0.02 \pm 0.01) \text{ mas yr}^{-1}, \end{cases}$$

for RGB-Mint stars:

$$\begin{cases} \langle \mu_\alpha \cos \delta \rangle = (0.03 \pm 0.01) \text{ mas yr}^{-1} \\ \langle \mu_\delta \rangle = (-0.01 \pm 0.01) \text{ mas yr}^{-1}, \end{cases}$$

and for the RGB-a sample:

$$\begin{cases} \langle \mu_\alpha \cos \delta \rangle = (0.05 \pm 0.03) \text{ mas yr}^{-1} \\ \langle \mu_\delta \rangle = (-0.01 \pm 0.04) \text{ mas yr}^{-1}. \end{cases}$$

We found no evidence for the presence of differences among the relative proper motions of the three RGB sub-populations at the level of 0.05 mas yr^{-1} in $\mu_\alpha \cos \delta$ and of 0.04 mas yr^{-1} in μ_δ

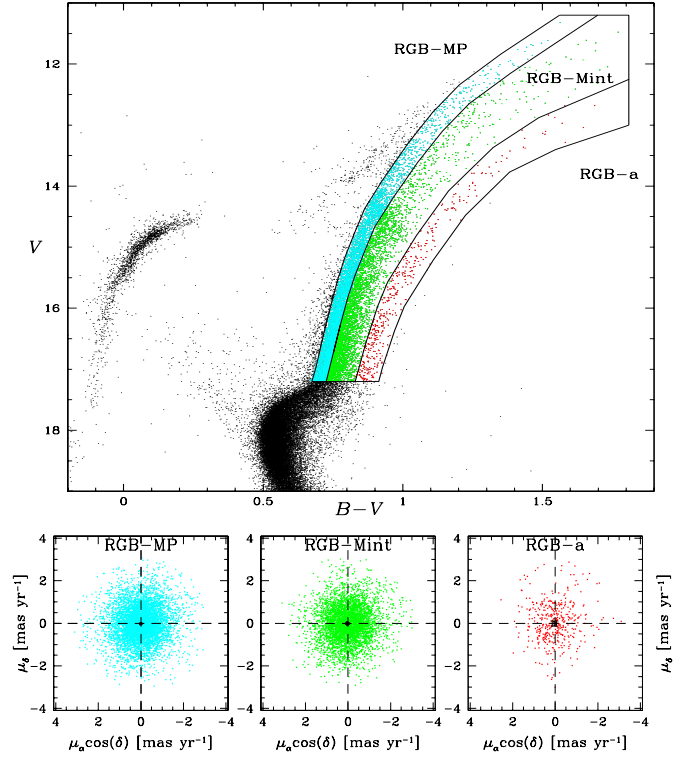


Fig. 13. (Top panel): V vs. $B - V$ CMD of proper-motion-selected member stars on which we defined three RGB subsamples: RGB-MP (cyan), RGB-Mint (green), and RGB-a (red). See text for the definition of the subpopulations. (Bottom panels): Proper motions of RGB-MP (left), RGB-Mint (middle), and RGB-a (right) subpopulations.

(i.e. relative tangential velocities of $\lesssim 1.3$, and $\lesssim 1.1 \text{ km s}^{-1}$, assuming a distance of 5.5 kpc for ω Cen). All three RGB subsamples exhibit the same mean proper motion, within the errors.

We therefore, agree with the results of both Platais et al. (2003) and Johnson et al. (2008) for RGB-a, and show that the RGB-Mint proper motion is also consistent with the other ω Cen sub-populations.

A final word on this issue requires an internal stellar proper-motion analysis, but suitable catalogs are not yet available.

6.2. Membership probability of published ω Cen variable stars

The study of variable stars in ω Cen can certainly benefit from our proper-motion catalog and cluster membership derivation.

Using the 1.0m Swope Telescope, Kaluzny et al. (2004) measured light curves of ~ 400 variable stars in ω Cen, 117 of which were new identifications. We cross-checked our proper-motion catalog with their own, and found a total of 338 variable stars in common, which had both V and B measurements in our catalog. In particular, there were 90 variable stars for which Kaluzny et al. (2004) did not provide B and/or V magnitudes. Our proper-motion catalog was also useful to locate these stars in the color-magnitude diagram. The position of the Kaluzny et al. (2004) variables in our CMD, as well as their membership probability, is shown in the left panel of Fig. 14. Depending on our measured membership probability, we divide the Kaluzny et al. (2004) sample into three categories: (1) $P_\mu < 30\%$ (red squares); (2) $30\% \leq P_\mu < 80\%$ (green triangles); and (3) $P_\mu \geq 80\%$ (blue

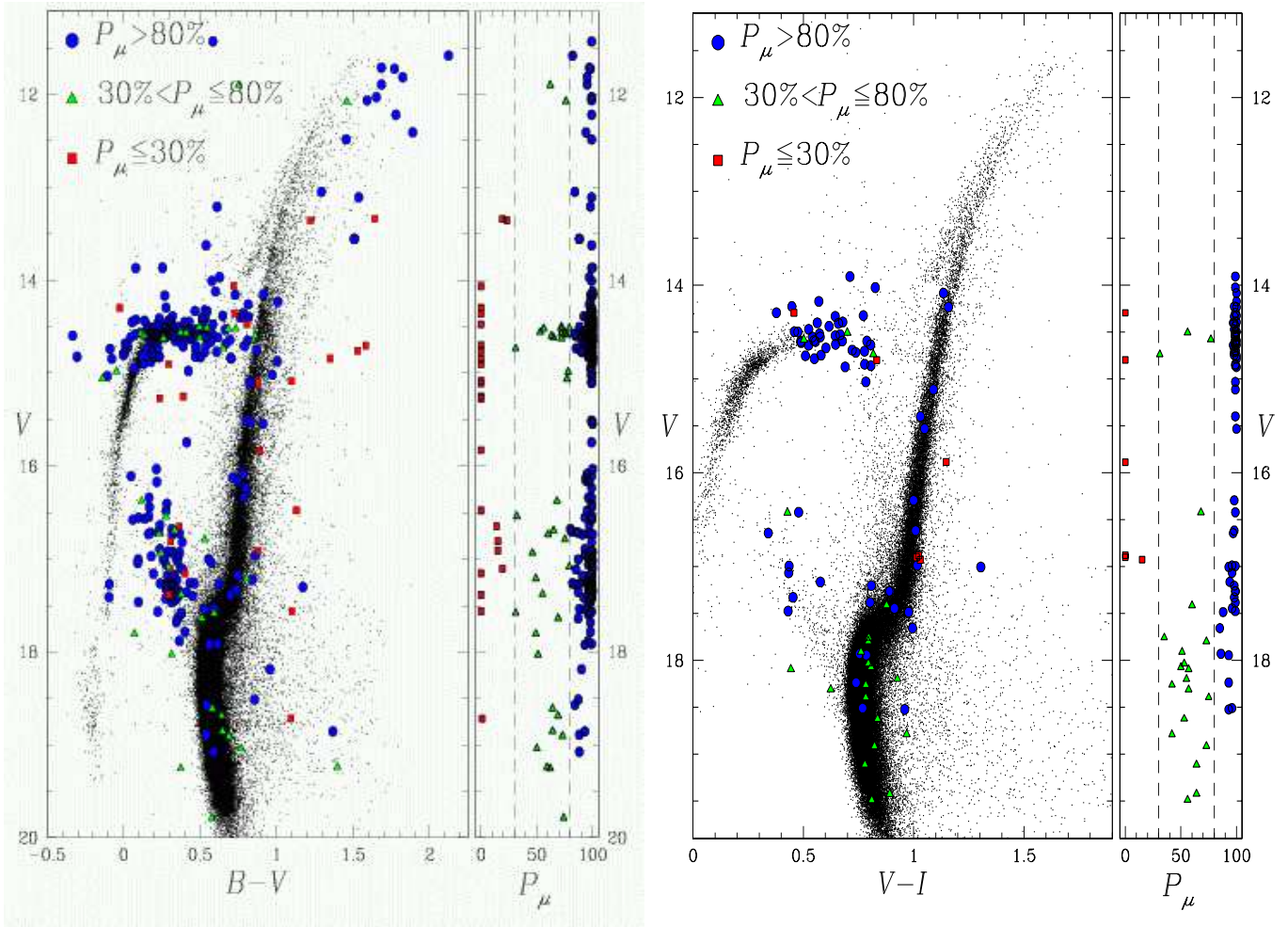


Fig. 14. (Left): ω Cen CMD with the cross-checked variable stars from the Kaluzny et al. (2004) catalog; red squares mark stars with a membership probability $P_\mu < 30\%$; green triangles are stars with $30\% \leq P_\mu < 80\%$, while blue circles are those with a probability to be cluster members $P_\mu \geq 80\%$. The membership probability P_μ versus the V magnitude is also shown. (Right): comparison with Weldrake et al. (2007) catalog.

circles). Of the 117 new variable identifications, 112 are in common with our catalog. Of these 112 stars, 15 have $P_\mu < 30\%$, and therefore these are probably not cluster members. On the other hand, 19 of these new variables have $30\% \leq P_\mu < 80\%$ and their membership remains uncertain. The remaining 78 stars ($P_\mu \geq 80\%$) are almost certainly ω Cen members. In Table 3, we report the membership probability values for all Kaluzny et al. (2004) variable stars identified in our catalog. New Kaluzny et al. (2004) identifications have their IDs starting with “N”.

The Kaluzny et al. (2004) variable star catalog was cross-checked with the X-ray sources detected by the XMM-Newton analysis presented by Gendre et al. (2003). For the 9 stars in common (see also Table 2 of Kaluzny et al. 2004), we can now provide (see Table 4) a membership probability based on our proper-motion analysis. A quick glance at Table 4 allows us to infer that only NV383 and NV369 are very likely cluster members, whereas the remaining 7 stars are most probably field population.

Using the 1.0m Telescope of the Australian National University, Weldrake et al. (2007) detected a total of 187 variable stars covering a wide area around ω Cen. These stars were matched with the Kaluzny et al. (2004) catalog, and 81 variable stars were found to be new discoveries. A cross-check of our catalog with that of Weldrake et al. (2007) provided 102

variable stars in common. Their location in the V versus $V - I$ CMD is shown in the right panel of Fig. 14. As completed for the Kaluzny et al. (2004) sample, different symbols mark different membership probability ranges, and Table 5 reports our membership probability for the Weldrake et al. (2007) variable catalog. Of the 81 Weldrake et al. (2007) new variable stars, 16 have counterparts in our proper-motion catalog. Four of these new variables are clearly not cluster members. These field objects include a detached eclipsing binary (V59), and three long-period variables (V31, V125, and V126).

Table 4. Membership probability of XMM-Newton X-Ray counterparts candidates. The IDs refer to Kaluzny et al. work.

ID _K	P_μ	ID _K	P_μ
NV367	0	NV376	0
NV375	0	NV377	0
V167	23	NV369	94
V223	0	NV383	99
NV378	31		

Table 3. Membership probability for the Kaluzny et al. (2004) variable star catalog. ID_K are the Kaluzny identification labels, while ID_{fw} refer to this work.

ID_K	P_μ	ID_{fw}	ID_K	P_μ	ID_{fw}	ID_K	P_μ	ID_{fw}	ID_K	P_μ	ID_{fw}	ID_K	P_μ	ID_{fw}	ID_K	P_μ	ID_{fw}
V1	99	290466	V66	99	311494	V132	96	184072	V214	97	42989	NV296	99	356415	NV354	97	263543
V2	74	271987	V67	99	352882	V135	97	181199	V216	99	155556	NV297	32	250290	NV355	93	196052
V3	99	248511	V68	100	345639	V136	99	213549	V217	98	218342	NV298	100	87382	NV356	49	206069
V4	97	279540	V70	98	93459	V137	99	225149	V218	96	358729	NV299	98	310461	NV357	92	158687
V5	100	298983	V71	99	209884	V139	90	215311	V219	88	347441	NV300	98	284928	NV358	99	129801
V8	99	200194	V74	100	360819	V141	100	177819	V220	100	321724	NV301	96	170554	NV359	46	222238
V9	100	238167	V75	99	352935	V142	65	193092	V221	96	320315	NV302	19	252220	NV360	100	118132
V10	98	273997	V76	100	340408	V143	90	217472	V223	0	355759	NV303	98	145690	NV361	64	234998
V11	99	302079	V77	99	316247	V144	95	201059	V224	99	349215	NV304	98	341374	NV363	93	321474
V12	99	283465	V78	0	243506	V145	91	143665	V225	96	274338	NV305	0	343091	NV364	93	243121
V13	99	259326	V81	99	270509	V146	72	177889	V226	99	167657	NV306	96	198996	NV365	0	71679
V14	97	26311	V82	99	236315	V147	97	143269	V227	98	287148	NV307	82	211960	NV366	97	132355
V15	100	273754	V83	99	323500	V148	95	209005	V228	96	92375	NV308	98	327308	NV367	0	350053
V16	100	40312	V85	98	292312	V150	100	58317	V229	97	285982	NV309	85	193994	NV368	0	349013
V17	99	261135	V86	99	242948	V152	82	177559	V231	99	59688	NV310	15	127228	NV369	94	124330
V18	98	267824	V87	97	255154	V153	100	238719	V233	99	336053	NV311	91	170132	NV370	0	358442
V19	100	205260	V88	94	261450	V154	96	155744	V234	0	157490	NV312	95	183516	NV372	93	290428
V20	99	204861	V90	89	239287	V155	98	272492	V235	87	309505	NV313	98	134090	NV373	59	300775
V21	99	246994	V91	92	241579	V156	99	128871	V236	85	282601	NV314	85	163946	NV374	99	312254
V22	99	86072	V92	99	327526	V157	98	221081	V237	99	286453	NV315	60	267539	NV375	0	349760
V23	100	273446	V94	98	305927	V158	31	153087	V238	99	179489	NV316	99	142842	NV376	0	189233
V24	99	84169	V95	94	188847	V161	76	149737	V239	99	179912	NV317	100	361100	NV377	0	324933
V25	99	199162	V96	63	225607	V162	97	108440	V240	99	239985	NV318	98	246801	NV378	31	341736
V26	98	226616	V97	99	256623	V163	100	337663	V241	1	289203	NV319	94	145544	NV379	99	328605
V27	96	201410	V98	99	227653	V164	99	334394	V242	98	171250	NV320	99	80363	NV380	96	148727
V29	62	191401	V99	99	210796	V165	85	227981	V249	99	236550	NV321	87	209026	NV381	0	311380
V30	99	168094	V100	77	215927	V166	72	241584	V250	92	62410	NV322	93	214126	NV382	96	343538
V32	100	322448	V101	99	169863	V167	23	87332	V251	97	231812	NV323	65	265232	NV383	99	336713
V33	98	184952	V102	100	162564	V168	0	124934	V252	98	187128	NV324	68	154689	NV384	93	46225
V34	99	103189	V103	98	195140	V169	99	285765	V253	99	209800	NV325	80	163821	NV385	99	35533
V35	99	309218	V104	99	92705	V184	100	134524	V254	99	214031	NV326	98	268304	NV386	98	218806
V38	98	52122	V105	98	111797	V185	99	320506	V258	99	253920	NV327	14	235193	NV387	96	190420
V39	99	76656	V106	99	202932	V186	94	200024	V259	99	177256	NV328	69	129813	NV388	0	205940
V40	99	150793	V107	100	147114	V187	91	107554	V261	98	324469	NV329	51	235596	NV389	49	169916
V41	72	145915	V108	99	178628	V188	95	160942	V263	100	243242	NV330	64	271511	NV390	100	262766
V42	88	177086	V109	99	174888	V189	99	175684	V264	98	157202	NV331	69	244602	NV391	99	46483
V43	99	227377	V110	100	164532	V190	99	243006	V265	98	192064	NV332	84	177605	NV393	99	36249
V44	100	78476	V111	95	193829	V191	99	301765	V266	85	206486	NV333	62	192856	NV394	95	81813
V45	98	219445	V112	78	158996	V192	100	319396	V267	99	234518	NV334	88	183248	NV395	88	177086
V46	99	249013	V113	99	130486	V193	99	318939	V268	99	243048	NV335	99	362118	NV397	94	244021
V47	99	281501	V114	97	159704	V194	99	128211	V270	98	164847	NV336	96	106751	NV398	96	267455
V48	98	158259	V115	99	83123	V195	81	274973	V271	98	165504	NV337	97	118163	NV399	98	165850
V49	99	36832	V116	56	204728	V197	79	126226	V272	99	248016	NV338	98	136414	NV400	99	129220
V50	99	214772	V117	75	179957	V198	55	145299	V273	99	223751	NV339	99	169580	NV401	98	130105
V51	99	278945	V118	96	160390	V199	87	194465	V274	77	305738	NV340	97	216161	NV402	87	52179
V52	53	205670	V119	91	140617	V200	75	243370	V275	94	214740	NV341	94	191217	NV403	0	229293
V53	99	56123	V120	99	110236	V201	99	369578	V276	99	101192	NV342	99	199357	NV404	99	244779
V54	98	352756	V121	97	129294	V203	100	372023	V277	99	217316	NV343	99	174660	NV405	88	252122
V56	98	38620	V122	99	105971	V204	99	45537	V280	99	300999	NV344	99	271739	NV406	100	292866
V57	100	48194	V123	100	44090	V205	96	302520	V285	99	74726	NV345	87	174082	NV407	88	309849
V58	96	284348	V124	99	26731	V206	97	57769	V288	99	289087	NV346	90	202477	NV408	50	234623
V59	96	171211	V125	99	14416	V207	98	297708	V289	99	324714	NV347	79	211972	NV409	73	322122
V60	99	110456	V126	99	15927	V208	97	244408	V291	98	97939	NV349	88	212595	NV410	0	180157
V61	100	216835	V127	99	193936	V209	99	297731	V292	98	129991	NV350	84	149574			
V62	99	208493	V128	100	162142	V210	15	58394	V293	99	85152	NV351	84	215235			
V64	99	54131	V129	19	185687	V211	90	298164	NV294	97	265591	NV352	99	183506			
V65	0	50869	V131	100	173358	V212	99	293439	NV295	99	340398	NV353	72	208251			

7. Summary

We have applied the photometric and astrometric technique developed by Anderson et al. (2006, Paper I) to the most puzzling globular cluster of the Milky Way: ω Centauri.

Based on CCD observations taken with only four years of temporal base-line, our measurements provide accurate proper motions to $B \sim 20$, four magnitudes deeper than the

photographic catalog of vL00. We have minimized the sky-concentration effects in our photometry. We provide a membership probability for all stars. Our catalog contains almost 360 000 stars with measured proper motion, and covers a wide area ($\sim 33 \times 33$ arcmin²) around the cluster center. In Fig. 15, we show a summary of our photometric catalog: we plot several ω Cen CMDs, derived with all the available filters and different color-baselines (top and middle rows). Plotted stars have a mem-

Table 5. Membership probability for the Weldrake et al. (2007) variable star catalog. ID_W are Weldrake et al. identification labels, ID_{rw} come from this work. The symbol (*) marks new Weldrake et al. identifications.

ID _W	P_μ	ID _{rw}	ID _W	P_μ	ID _{rw}	ID _W	P_μ	ID _{rw}	ID _W	P_μ	ID _{rw}	ID _W	P_μ	ID _{rw}	ID _W	P_μ	ID _{rw}
V31*	0	234574	V48	100	360819	V102	15	58394	V119	51	126839	V142	42	208115	V160*	73	292364
V32	99	236315	V59*	0	23863	V103	99	54131	V120	68	154689	V143	98	201164	V161	73	322122
V33	100	205260	V60	48	40133	V104	93	46225	V121	53	159019	V144*	100	247143	V162	99	311494
V34	99	239985	V61	100	48194	V105	99	83123	V122	100	162685	V145*	99	270697	V163	93	321474
V35	56	214167	V62	97	42989	V106	100	78476	V123	99	155556	V146	100	243242	V164	99	327526
V36	98	267824	V63	99	86072	V107	99	103189	V124	75	137352	V147	99	246994	V165	99	320506
V37	0	243506	V64	99	84169	V108	48	92977	V125*	0	127167	V148	77	305738	V166	31	341736
V38	99	270509	V65	99	128211	V109	99	110456	V126*	0	85789	V150	50	302398	V167	100	345639
V39	100	292866	V66	98	111797	V110	99	105971	V133	94	201061	V151	2	283256	V168	64	347475
V40	99	289620	V67	98	93459	V111	99	110236	V134	53	234700	V152	100	298983	V169	100	337663
V41	99	293439	V68*	99	120134	V112	86	153744	V135	85	205826	V153	65	297730	V170	99	352882
V42	99	285765	V69*	98	108406	V113	98	136502	V136	50	228136	V154	98	287148	V171	98	352756
V43	99	324714	V70	100	162564	V114	55	160877	V137	42	225221	V155	64	283990	V172	96	358729
V44*	93	328996	V71*	88	132518	V115	57	158023	V138	99	251061	V156	97	279540	V173	98	219445
V45	99	316247	V72*	73	133191	V116	60	141176	V139	56	204728	V157*	96	273996	V174	99	249013
V46*	96	320258	V81*	96	6069	V117	97	129294	V140	57	224813	V158	98	273997	V176	98	292312
V47	99	352935	V101	99	36832	V118	35	151268	V141	51	218172	V159*	93	287079	V178	36	309751

bership probability of $P_\mu > 90\%$. Photometric errors range from 0.02 mag for brighter stars to 0.05 mag for the fainter ones. In the bottom panels of Fig. 15, we show the SGB region of ω Cen in the B versus $B-R$ CMD on the left, and two color-color diagrams with different colors on the right.

The high precision of our astrometry and multi-band photometry once again emphasizes the importance of accurate representation of the PSF across the entire field-of-view, especially for wide-field imagers, exemplified by the concept of empirical PSF (Paper I).

The primary aim of this work is, of course, to provide wide-field membership probability measurements for spectroscopic follow-up studies, down to the turn-off region of the cluster. However, the high quality of our photometric and astrometric measurements also provide a crucial observational constraint of the multiple ω Cen sub-populations. Due to our proper-motion-selected RGB sub-populations, we can confirm that the metal-poor, metal-intermediate, and metal-rich components have the same proper motions which is that of ω Cen, within our measurements uncertainties.

We finally provide membership probability determinations for the Kaluzny et al. (2004) and Weldrake et al. (2007) ω Cen variable star catalogs.

7.1. Electronic catalog

The catalog is available at the SIMBAD on-line database². Description of the catalog: column (1) contains the ID; columns (2) and (3) give the J2003.29 equatorial coordinates in decimal degrees; columns (4) and (5) provide the pixel coordinates x and y of the distortion-corrected reference meta-chip. Columns (6) and (7) contain the proper-motion values along $\mu_\alpha \cos \delta$ in units of mas yr⁻¹, with the corresponding r.m.s.; columns (8) and (9) provide the proper-motion values along μ_δ , with the corresponding r.m.s., in the same units. Columns from (10) to (21) give the photometric data, i.e. $U, B, V, R_C, I_C, H_\alpha$ magnitudes and their errors. The last two columns give the proper-motion membership probability $P_\mu(1)$ for all the stars (22), and for a sub-sample of 120,259 stars with the alternative membership determination

$P_\mu(2)$ (23). In this case, if the second membership determination is not provided, we flag it with the value -1.

If photometry in a specific band is not available, a flag equal to 99.999 is set for magnitude and error.

Table 6 contains the first lines of the on-line catalog.

Acknowledgements. A. Bellini acknowledges the support by the CA.RI.PA.RO. foundation, and the STScI under the 2008 graduate research assistantship program. I. Platais gratefully acknowledges support from the National Science Foundation through grant AST 04-06689 to Johns Hopkins University and by NASA grant *HST*-AR-09958.01-A, awarded by the Space Telescope Institute, which is operated by the Association of Universities for Research in Astronomy, Inc., under NASA contract NAS5-26555. We thank Floor van Leeuwen for his help in providing us a complete version of his catalog as well as stimulating discussions. We thank the anonymous referee for the careful reading of the manuscript, and for the useful comments.

References

- Andersen, M. I., Freyhammer, L., & Storm, J. 1995, *Calibrating and Understanding HST and ESO Instruments*, 87
- Anderson, J., 1997, ph.D. thesis, Univ. California, Berkeley
- Anderson, J., 2003, in *ASP. Conf. Ser. 296, New Horizons in Globular Cluster Astronomy*, ed. G. Piotto, G. Meylan, D. Djorgovski, & M. Rieello (San Francisco: ASP), 125
- Anderson, J., & King, I. R. 2003, *PASP*, 115, 113
- Anderson, J., Bedin, L. R., Piotto, G., Yadav, R. S., & Bellini, A. 2006, *A&A*, 454, 1029, (Paper I)
- Anderson, J. et al. 2008, *AJ*, 135, 2055
- Balaguer-Núñez, L., Tian, K. P., & Zhao, J. L. 1998, *A&AS*, 133, 387
- Bedin, L. R., Piotto, G., Anderson, J., Cassisi, S., King, I. R., Momany, Y., & Carraro, G. 2004, *ApJ*, 605, L125
- Bedin, L. R., Cassisi, S., Castelli, F., Piotto, G., Anderson, J., Salaris, M., Momany, Y., & Pietrinferni, A. 2005, *MNRAS*, 357, 1038
- Bessell, M. S., & Norris, J. 1976, *ApJ*, 208, 369
- Butler, D., Dickens, R. J., & Epps, E. 1978, *ApJ*, 225, 148
- Calamida, A., et al. 2005, *ApJ*, 634, L69
- Calamida, A., Corsi, C. E., Bono, G., Stetson, P. B., Freyhammer, L. M., & Buonanno, R. 2008, *ArXiv e-prints*, 801, arXiv:0801.0693
- Cassisi, S., Schlattl, H., Salaris, M., & Weiss, A. 2003, *ApJ*, 582, L43
- Del Principe, M., et al. 2006, *ApJ*, 652, 362
- Ferraro, F. R., Bellazzini, M., & Pancino, E. 2002, *ApJ*, 573, L95
- Ferraro, F. R., Beccari, G., Rood, R. T., Bellazzini, M., Sills, A., & Sabbi, E. 2004, *ApJ*, 603, 127
- Freeman, K. C., & Rodgers, A. W. 1975, *ApJ*, 201, L71
- Gendre, B., Barret, D., & Webb, N. A. 2003, *A&A*, 400, 521
- Harris, W. E. 1996, *AJ*, 112, 1487
- Hilker, M., Kayser, A., Richtler, T., & Willemsen, P. 2004, *A&A*, 422, L9

² <http://simbad.u-strasbg.fr/simbad/>

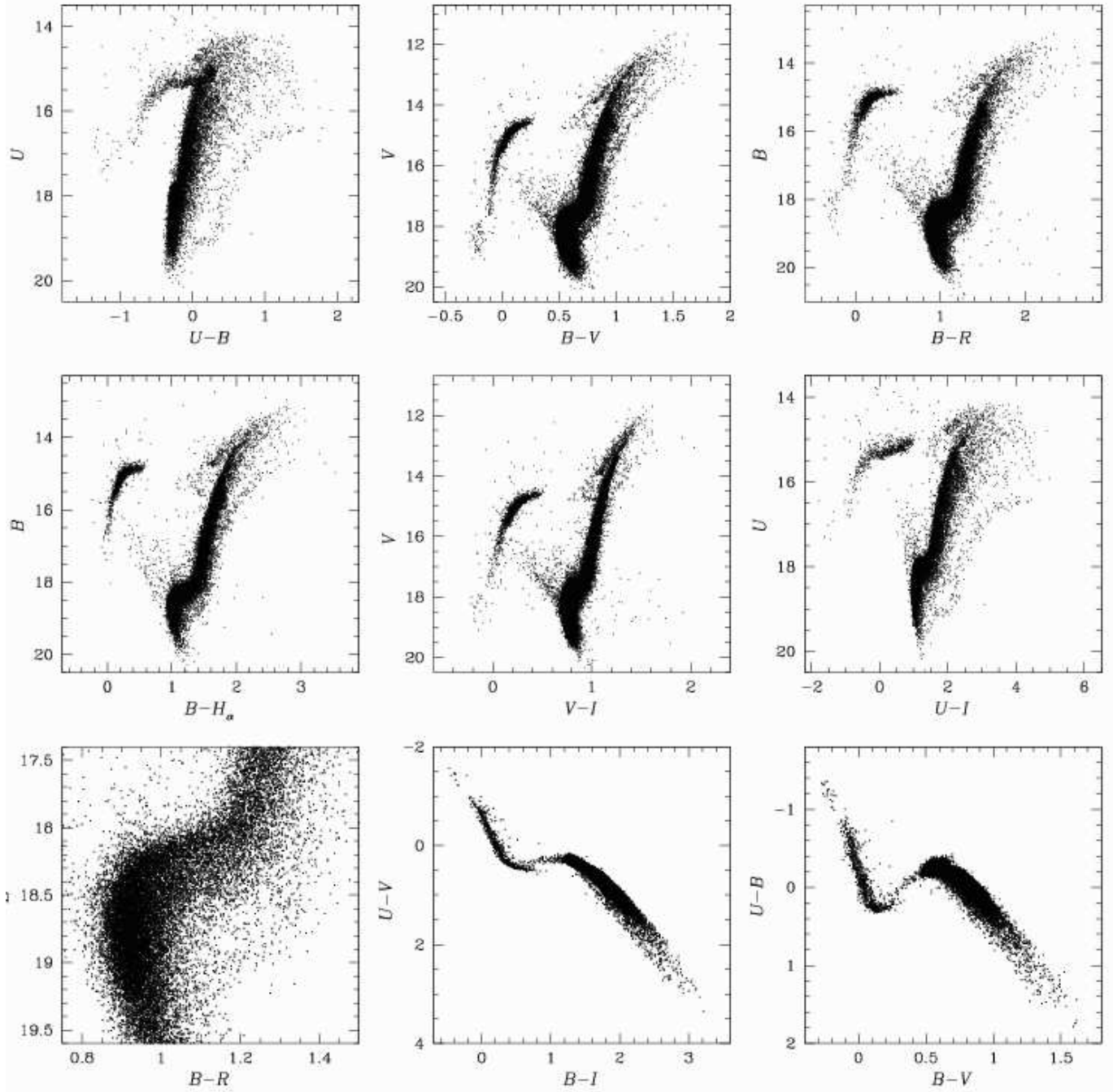


Fig. 15. (Top): membership probability selected ($P_\mu > 90\%$) ω Cen CMDs. From left to right U vs. $(U-B)$, V vs. $(B-V)$, and B vs. $(B-R)$. Plotted stars have photometric errors going from 0.02 mag for the brighter to 0.05 for the faintest ones. (Middle): same star selection criteria. From left to right: B vs. $(B-H_\alpha)$, V vs. $(V-I)$, and U vs. $(U-I)$. (Bottom): the B vs. $(B-R)$ CMD, zoomed in the SGB region, is shown on the left. The two plots on the right show two color-color diagrams obtained from different filters.

Hughes, J., Wallerstein, G., van Leeuwen, F., Hilker, M. 2004, *AJ*, 127, 980
 Johnson, C. I., Pilachowski, C. A., Simmerer, J., & Schwenk, D. 2008, *ArXiv e-prints*, 804, arXiv:0804.2607, *ApJ* accepted
 Kaluzny, J., Olech, A., Thompson, I. B., Pych, W., Krzemiński, W., & Schwarzenberg-Czerny, A. 2004, *A&A*, 424, 1101
 Koch, A., Odenkirchen, M., Grebel, E. K., & Caldwell, J. A. R. 2004, *Astronomische Nachrichten*, 325, 299
 Lee, Y.-W., Joo, J.-M., Sohn, Y.-J., Rey, S.-C., Lee, H.-C., & Walker, A. R. 1999, *Nature*, 402, 55
 Manfroid, J., & Selman, F. 2001, *The Messenger*, 104, 16
 Merritt, D., Meylan, G., & Mayor, M. 1997, *AJ*, 114, 1074
 Meylan, G., Mayor, M., Duquenois, A., & Dubath, P. 1995, *A&A*, 303, 761

Momany, Y., Cassisi, S., Piotto, G., Bedin, L. R., Ortolani, S., Castelli, F., & Recio-Blanco, A. 2003, *A&A*, 407, 303
 Monet, D. G., Dahn, C. C., Vrba, F. J., Harris, H. C., Pier, J. R., Luginbuhl, C. B., & Ables, H. D. 1992, *AJ*, 103, 638
 Norris, J., & Bessell, M. S. 1975, *ApJ*, 201, L75
 Norris, J., & Bessell, M. S. 1977, *ApJ*, 211, L91
 Norris, J. E., & Da Costa, G. S. 1995, *ApJ*, 441, L81
 Norris, J. E., Freeman, K. C., & Mighell, K. J. 1996, *ApJ*, 462, 241
 Norris, J. E., 2004, *ApJ*, 612, 25
 Pancino, E., Ferraro, F. R., Bellazzini, M., Piotto, G., & Zoccali, M. 2000, *ApJ*, 534, L83
 Pancino, E., Galfo, A., Ferraro, F. R., & Bellazzini, M. 2007, *ApJ*, 661, L155
 Piotto, G., et al. 2005, *ApJ*, 621, 777

- Platais, I., Wyse, R. F. G., Hebb, L., Lee, Y.-W., & Rey, S.-C. 2003, *ApJ*, 591, L127
- Rey, S.-C., Lee, Y.-W., Ree, C. H., Joo, J.-M., Sohn, Y.-J., & Walker, A. R. 2004, *AJ*, 127, 958
- Sanders, W. L. 1971, *A&A*, 14, 226
- Sarajedini, A., et al. 2007, *AJ*, 133, 290
- Selman, F. J., 2001, "Determining a zero-point variation map for the WFI" (<http://www.lis.eso.org/lasilla/Telescopes/2p2T/E2p2M/WFI/zeropoints>)
- Selman, F. J., & Melnick, J. 2005, *A&A*, 443, 851
- Sirianni, M., et al. 2005, *PASP*, 117, 1049
- Sollima, A., Pancino, E., Ferraro, F. R., Bellazzini, M., Straniero, O., & Pasquini, L. 2005, *ApJ*, 634, 332
- Stanford, L. M., Da Costa, G. S., Norris, J. E., and Cannon R. D., 2006, *ApJ*, 647, 1075
- Stetson, P. B. 2000, *PASP*, 112, 925
- Stetson, P. B. 2005, *PASP*, 117, 563
- Suntzeff, N. B., & Kraft, R. P. 1996, *AJ*, 111, 1913
- Tian, K.-P., Zhao, J.-L., Shao, Z.-Y., & Stetson, P. B. 1998, *A&AS*, 131, 89
- van de Ven, G., van den Bosch, R. C. E., Verolme, E. K., & de Zeeuw, P. T. 2006, *A&A*, 445, 513
- van Leeuwen, F., Le Poole, R. S., Reijns, R. A., Freeman, K. C., & de Zeeuw, P. T. 2000, (vL00) *A&A*, 360, 472
- Vasilevskis, S., Klemola, A., & Preston, G. 1958, *AJ*, 63, 387
- Villanova, S., et al. 2007, *ApJ*, 663, 296
- Weldrake, D. T. F., Sackett P.D., & Bridges T. J., 2007, *AJ*, 133, 1447
- Yadav, R. K. S., Bedin, L. R., Piotto, G., Anderson, J., Villanova, S., Platais, I., Pasquini, L., Momany, Y., & Sagar, R. 2008, *A&A*, 484, 609, (Paper II)
- Zacharias, N., Urban, S. E., Zacharias, M. I., Wycoff, G. L., Hall, D. M., Monet, D. G., & Rafferty, T. J. 2004, *AJ*, 127, 3043
- Zhao, J. L., & He, Y. P. 1990, *A&A*, 237, 54

ID	α	δ	x	y	$\mu_\alpha \cos \delta$	$\sigma_{\mu_\alpha \cos \delta}$	μ_δ	σ_{μ_δ}	U	σ_U	B	σ_B	V	σ_V	R	σ_R	I	σ_I	H_α	σ_{H_α}	$P_\mu(1)$	$P_\mu(2)$
(1)	(2)	(3)	(4)	(5)	(6)	(7)	(8)	(9)	(10)	(11)	(12)	(13)	(14)	(15)	(16)	(17)	(18)	(19)	(20)	(21)	(22)	(23)
[#]	[°]	[°]	[pixel]	[pixel]	[mas/yr]	[mas/yr]	[mas/yr]	[mas/yr]	[mag]	[mag]	[mag]	[mag]	[mag]	[mag]	[mag]	[mag]	[mag]	[mag]	[mag]	[mag]	[%]	[%]
1	201.802078	-47.750278	3016.264	-93.270	-3.25	0.52	11.78	6.12	99.999	99.999	20.535	0.056	19.842	0.155	19.332	0.219	18.729	0.071	99.999	99.999	0	28
2	201.763730	-47.750272	3407.004	-93.189	7.26	8.23	1.98	3.16	99.999	99.999	19.254	0.064	18.681	0.044	18.214	0.063	17.909	0.033	99.999	99.999	69	-1
3	201.799369	-47.750242	3043.872	-92.734	-0.41	14.48	7.24	6.54	99.999	99.999	21.173	0.080	20.441	0.046	19.854	0.044	19.437	0.058	99.999	99.999	39	-1
4	201.641896	-47.750155	4648.364	-92.553	11.20	8.53	9.50	6.65	99.999	99.999	20.938	0.060	20.242	0.083	19.708	0.051	19.308	0.081	99.999	99.999	43	-1
5	201.611638	-47.750119	4956.656	-92.562	0.43	0.63	11.93	3.89	99.999	99.999	17.145	0.015	16.632	0.016	16.238	0.007	15.953	0.035	99.999	99.999	19	0
6	201.609219	-47.750121	4981.298	-92.651	-1.55	6.82	1.60	7.53	99.999	99.999	20.856	0.036	20.202	0.064	19.660	0.040	19.263	0.047	99.999	99.999	57	-1
7	201.506294	-47.749911	6029.910	-92.178	6.71	5.49	21.84	4.47	99.999	99.999	19.905	0.033	19.095	0.031	18.552	0.039	18.136	0.060	99.999	99.999	0	-1
8	201.721527	-47.750125	3837.015	-91.161	1.23	3.45	7.76	9.23	99.999	99.999	20.844	0.057	20.116	0.017	19.692	0.068	19.347	0.069	99.999	99.999	62	-1
9	201.714951	-47.750153	3904.018	-91.634	5.27	3.52	2.33	6.89	99.999	99.999	20.354	0.050	19.696	0.028	19.261	0.051	18.909	0.032	99.999	99.999	70	-1
10	201.629034	-47.750053	4779.417	-91.229	4.24	3.80	7.46	1.69	99.999	99.999	19.275	0.024	18.694	0.024	18.310	0.030	17.953	0.057	99.999	99.999	0	55
[...]	[...]	[...]	[...]	[...]	[...]	[...]	[...]	[...]	[...]	[...]	[...]	[...]	[...]	[...]	[...]	[...]	[...]	[...]	[...]	[...]	[...]	[...]

Table 6. First lines of the electronically available catalog.